J. Fluid Mech. (2025), *vol.* 1019, A38, doi:10.1017/jfm.2025.10558

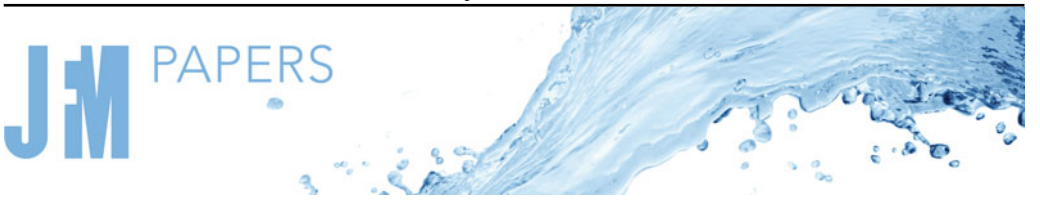

The effect of turbulence on a flexible finite wing: forces, deflections and the wingtip vortex

Srikar Yadala[1], **Simon Dehareng**[1,2], **Ingrid Neunaber**[1,3], **Girish K. Jankee**[1], **Rene Kaufmann**[4], **Marie Couliou**[5] and **R. Jason Hearst**[1]

[1]Department of Energy & Process Engineering, Norwegian University of Science & Technology, NO-7491 Trondheim, Norway

[2]Department of Aerospace and Mechanical Engineering, University of Liège, Liège 4000, Belgium

[3]FLOW, Department of Engineering Mechanics, KTH Royal Institute of Technology, Stockholm SE-100 44, Sweden

[4]Department of Structural Engineering, Norwegian University of Science & Technology, Trondheim, NO-7491, Norway

[5]DAAA, ONERA, Institut Polytechnique de Paris, Meudon 92190, France

Corresponding authors: Srikar Yadala, srikar.y.venkata@ntnu.no; R. Jason Hearst, jason.hearst@ntnu.no

(Received 14 October 2024; revised 21 June 2025; accepted 2 August 2025)

The impact of freestream turbulence (FST) on the aerodynamic performance of a flexible finite wing and the produced wingtip vortex was investigated. The wing had a NACA 4412 airfoil profile and the chord-based Reynolds number was 1.4×10^5. The experiments were conducted in a closed-loop wind tunnel with four different inflow turbulence intensities (0.2 %, 3 %, 8 % and 13 %) generated using an active turbulence grid. Force balance measurements revealed that increasing the scale of the FST increased the maximum lift and delayed stall. Digital image correlation (DIC) measured deflections of the wing's structure. Spanwise bending was found to be the dominant deformation. While the wing vibrated at its natural frequency in all conditions, FST increased the amplitude of the vibrations. A similar spectral signature was observed in the lift force fluctuations as well. Stereoscopic particle image velocimetry measurements were obtained two chord lengths downstream of the trailing edge simultaneously with DIC. FST decreased the vortex strength, and marginally increased vortex diffusion and size. It also increased the vortex meandering amplitude, while reducing the meandering frequency band. For the cases with a turbulence intensity of 8 % and 13 %, the frequency of meandering and the wing's vibration were similar and a phase relation between the two motions was observed. Proper orthogonal decomposition of the vortex (after removing meandering) and the subsequent

velocity field reconstruction revealed temporal fluctuations in the vortex strength at the same frequency as the wing's vibration. This was linked to the lift force fluctuations induced by the wing's deformations.

Key words: flow-structure interactions, turbulent flows, vortex dynamics

1. Introduction

This study aims to better understand the effects of homogeneous isotropic turbulence on a flexible finite wing and the resulting wingtip vortex in its wake. Ambient or freestream turbulence (FST) is a crucial factor for any flying engine. Commercial aircraft encounter atmospheric boundary layer effects during landing and take-off phases, as well as high-altitude turbulence while cruising (Sarpkaya & Daly 1987). As aerostructures become lighter and more flexible, the loads caused by FST are gaining importance (Dowell, Edwards & Strganac 2003) and the influence of flexible-body response on these loads cannot be neglected. The influence of ambient turbulence is, in particular, an important parameter for microengines operating on micro-UAVs (unmanned aerial vehicles) (see for example Kroo *et al.* 2001 and Norihisa & Isao 2002) in complex aerodynamic conditions. In urban environments turbulence levels can reach the range of 10 %–20 %, with length scales of up to 10 times the order-of-magnitude of the aircraft's chord (Watkins *et al.* 2006). Airfoils also experience FST in applications such as turbomachines and wind turbines. As explained by Vita *et al.* (2020), wind-turbine performance can be drastically affected in turbulent environments and especially urban turbulence. Moreover, the fatigue loads acting on wind turbines also increase with FST (Vermeer & Crespo 2003). As such, further insights into the interaction of FST with flexible finite-length wings have broad applications, particularly in aeronautics and wind turbine design.

The effects of FST on the aerodynamic performance of an airfoil are numerous. The existing literature is generally focused on extruded two-dimensional (2-D) geometries (or infinite wings) rather than finite-wing models (studies of the latter are discussed later). For the case of 2-D airfoils, the addition of FST leads to an increase in the maximum lift in several studies (Hoffmann 1991; Vita *et al.* 2020; Li & Hearst 2021; Thompson *et al.* 2023, 2025). Contrarily, Kay, Richards & Sharma (2020) compared the effects of turbulence on two airfoils, a symmetric NACA0012 and a cambered NACA4412, over a range of Reynolds numbers (from 5.0×10^4 to 2.0×10^5) and turbulence intensities (from 1.3 % to 15 %) and found that increased turbulence intensity significantly decreased the maximum lift coefficient of the cambered airfoil, while it slightly increased the lift coefficient of the symmetrical airfoil. Lift fluctuations have also been observed to increase with FST in some studies (Vita *et al.* 2020; Thompson *et al.* 2023, 2025). Some studies demonstrate an increase in the lift-curve's slope (Li & Hearst 2021), while others observe no change (Hoffmann 1991; Wang *et al.* 2014). Similarly, while some report an increase in the stall angle (Hoffmann 1991; Vita *et al.* 2020; Thompson *et al.* 2023, 2025), others show no changes to the stall angle with the addition of turbulence (Li & Hearst 2021). The increased performance is attributed to the reduction (and sometimes the destruction) of the laminar separation bubble (Ifju *et al.* 2002; Sicot *et al.* 2006; Vita *et al.* 2020; Li & Hearst 2021). In such cases, the incoming homogenous FST keeps the boundary layer attached and suppresses the recirculation region which leads to a delay in the onset of stall as demonstrated by Thompson *et al.* (2023).

This brief review highlights the lack of consensus on how the forces experienced by 2-D wings are affected by the addition of FST. A more detailed summary of this issue is

Study	Airfoil	Measurement	Re_c ($\times 10^5$)	T_i (%)	α (°)	x/c
Devenport *et al.* (1996)	NACA 0012	HWA	5.30	0.10	5	4, 9, 14, 19, 24, 29
Chow *et al.* (1997)	NACA 0012	HWA	46.0	0.15	10	(−1.14, 0.678)
Heyes *et al.* (2004)	NACA 0012	PIV	1.00, 2.20	1	4, 6, 8, 10	22.9
Bailey *et al.* (2006)	NACA 0012	HWA	2.40	0.4, 2.5, 5	5	0.05, 1, 3, 5, 7, 9
Bailey & Tavoularis (2008)	NACA 0012	HWA	2.40	0.4, 2.5, 5	5	3, 5, 7, 9
Giuni & Green (2013)	NACA 0012	SPIV	7.40	0.4	0, 4, 12	−0.5, −0.25, 0.25, 1
Ahmadi-baloutaki *et al.* (2014)	NACA 0015	HWA	1.6	0.4	0 to 25	0.1, 0.42, 0.77, 1.03
Serrano-aguilera *et al.* (2016)	NACA 0012	PIV	0.5, 4.6	3	10	0, 1, 2, 3, 4, 5
Ghimire & Bailey (2017)	NACA 0012	PIV	0.12	0.4, 2.5, 5	8	—
Chen *et al.* (2018*a*)	NACA 0012	Volumetric PIV	0.5, 0.15	0.5	−10, −5, 5, 10	—
Ben Miloud *et al.* (2020)	NACA 0012	HWA, SPIV	2.00, 3.00	0.5, 3, 6	5	0.5, 2.5, 5.5, 7
Kay *et al.* (2020)	NACA 4412	Pressure taps	0.5 to 2	1.3 to 15	−6 to 20	—
Cruz Marquez *et al.* (2021*b*)	NACA 4412	SPIV	0.84 to 4.40	—	1 to 5.5	(0, 970)
Bölle *et al.* (2023)	NACA 0012	SPIV	1.70	0.5	9	2, 4, 12, 20, 26
Solis *et al.* (2024)	NACA 0012	PIV	0.2	—	0 to 12	[0, 20]
Present study	NACA 4412	SPIV	1.4	0.2, 3, 8, 13	5	2

Table 1. Summary of experimental set-ups of a selection of the previous investigations of the structure and behaviour of wingtip vortices. The listed studies were performed in either a wind tunnel or a towing tank. The downstream positions (x/c) are listed from the trailing edge; this required a change of origin compared with some of the source material.

provided by Li & Hearst (2021). In contrast, studies on the effect of FST on finite wings are far scarcer. In this regard, a mention must be made to the recent efforts of Zhang *et al.* (2020, 2022*a*,*b*), who studied the aerodynamic performance of a finite wing that is submerged in the wake of a bluff body. Such turbulent conditions lead to an increase in the maximum lift and a delay in the onset of stall as well. However, the effect of homogeneous isotropic turbulence on the forces experienced by finite wing geometries remains largely unexplored in the literature, and the results presented herein contribute to this growing body of knowledge.

The effect of FST has not only been investigated on the wing's performance itself, but also on the wake generated, and especially the resulting wingtip vortex. Numerous experimental studies (Sarpkaya & Daly 1987; Chow, Zilliac & Bradshaw 1997; Giuni & Green 2013; Serrano-Aguilera *et al.* 2016; Chen, Wang & Gursul 2018*a*; Cruz Marquez *et al.* 2021*a*; Bölle *et al.* 2023) have focused on the evolution of wingtip vortices, acknowledging their sensitivity to a myriad of factors including Reynolds number, angle of attack (α), ground proximity, atmospheric FST, buoyancy and wind shear. Key information of some of these experimental investigations are summarised in table 1. Bailey, Tavoularis & Lee (2006) showed that FST can reduce the strength of the wingtip

vortex and that the azimuthal velocity profiles were affected by wingtip vortex meandering; here, 'vortex meandering' is used to refer to the low-frequency random motion of the vortex axis in the transverse plane. Later, using hot-wire anemometry (HWA) in the same experimental set-up, Bailey & Tavoularis (2008) found that increasing FST increased both the rate of decay of the circumferential velocity and vortex meandering, while the radial velocity remained the same. Their results are in agreement with previous studies of Chow *et al.* (1997) and Heyes, Jones & Smith (2004). Ahmadi-Baloutaki, Carriveau & Ting (2014) performed analysis on a trailing vortex flow subjected to external turbulence on a NACA 0015 wing and demonstrated a correlation between the rise in the aerodynamic forces and the rise in the turbulent kinetic energy in the vortex flow field with FST. In a towing tank experiment, Ghimire & Bailey (2017) also observed that increasing the FST leads to faster decay of the vortex strength, faster decay of the peak azimuthal velocity and faster breakdown of the vortex itself. A year later, Bailey *et al.* (2018) demonstrated that the meandering amplitude (represented here by σ_i) and the core radius of the tip vortex (r_c) scaled with FST. Ben Miloud *et al.* (2020) also observed that both the meandering amplitude and the rate of decay of the wingtip vortex increased with FST, while the vortex strength decreased with FST. Finally, they found that the vortex development was nearly independent of $Re_c = U_\infty c/\nu$ (where U_∞ is the incoming freestream velocity, c is the airfoil chord and ν is the kinematic viscosity) and FST, as there was little variation in the vortex radius and peak vorticity levels for an increasing Re_c. Most recently, by analysing the main features of experimentally observed meandering, Bölle (2024) developed a Brownian-motion-like model within the framework of linear response theory to describe vortex meandering as a competition between external perturbations and intrinsic vortex dynamics, providing evidence of ergodic probability dynamics.

The previous studies mentioned above studied rigid wings. While minimal in number, some studies have tackled the effect of incoming gusts on aeroelastic or flexible wings (Tang, Grasch & Dowell 2010; Neumann & Mai 2013; Chen *et al.* 2018*b*; Fernandez, Cleaver & Gursul 2022; Mertens *et al.* 2023; Thompson *et al.* 2025). One area that has received limited attention in the existing literature is understanding how FST with large length scales influences the unsteady aerodynamic characteristics of a flexible wing and if such turbulent conditions can excite various structural modes. The potential relationship between the wing deflection and tip-vortex dynamics, especially its meandering, has also not been investigated. Chen & Jaworski (2020) reported simulations of inviscid interaction of a point vortex with a downstream airfoil which was elastically mounted and free to plunge in a single degree of freedom. It was shown that the trajectory of the point vortex depends on its strength and initial upstream location, as well as the airfoil's natural frequency. They suggested that the transient interaction may induce an oscillatory damping of airfoil circulation and plunge displacement. In an experimental study at a low Reynolds number of $Re_c = 2 \times 10^4$, Solis *et al.* (2024) observed that a deformation of $0.045c$ did not alter the general structure of the vortex. Chen *et al.* (2018*b*) conducted experiments where a wingtip vortex from an upstream wing impinged on a flexible finite wing. The wing's deformation was primarily bending, with a frequency near that of the vortex meandering. An increase in the meandering amplitude was also reported. However, the authors did not find any coupling between the wing's oscillations and the vortex meandering. Finally, a recent study that is closely related to the current investigation is that of Thompson *et al.* (2025) who studied the aerodynamic performance of, and the flow around, a flexible wing affected by homogenous isotropic turbulence. They too showed that the deflections induced in the wing were predominantly related to bending. Fluctuations in the forces noticeably increased and the spectral content of these fluctuations were related to the wing's deflections. While they did not study the tip vortex, the behaviour of the flow

around the wing was similar to their previous work with a rigid wing, i.e. the flow remained attached with the addition of FST and the recirculation region was suppressed (Thompson *et al.* 2023).

As stated at the beginning of this section, the objective of the present investigation is to gain a deeper understanding of the effects of approximately homogeneous and isotropic turbulence on the wingtip vortex shed from a flexible finite wing. This is a multifaceted problem that requires examining three key aspects: the impact of FST on the aerodynamic performance of a flexible wing, its influence on the wingtip vortex and the influence of wing's deflections on the dynamics of the tip vortex. Consequently, the study can be broken down into the following subtasks.

(i) The literature review highlights a lack of consensus on the effects of FST on the performance of 2-D airfoils to begin with. Moreover, studies investigating flexible finite wing geometries are extremely limited. Therefore, a key objective of this study is to gain a deeper understanding of the aerodynamic performance of the flexible wing and the deflections it undergoes when subjected to FST.
(ii) The second objective is to understand the behaviour of the wingtip vortex when it is exposed to FST, particularly at turbulence levels more representative of urban environments (above 10 %), which exceed those typically tested in the literature. This will also serve as an initial characterisation of the wingtip vortex shed by a flexible wing, and hints at how the wing's flexibility may influence the vortex dynamics.
(iii) Finally, the influence of the wing's deflections on the structure and dynamics of the wingtip vortex will be examined in detail, representing the ultimate goal of this study.

This article is organised as follows: § 2 describes the experimental facility and the measurement techniques employed. It also includes a detailed characterisation of the base flow (no wing) for the different turbulence cases investigated herein. The effect of FST on the wing, including its deflections and aerodynamic performance, is discussed in § 3. The ensuing wingtip vortex is characterised for different turbulent conditions using methodologies from the existing literature in § 4 (and Appendix A). The interplay between FST, the wing's induced vibrations and the dynamics of the tip vortex is examined in § 5 using the Hilbert transform and proper orthogonal decomposition (POD). Finally, the conclusions drawn from this study are presented in § 6.

2. Experimental set-up

2.1. *Wind tunnel and wing*

The experiments were conducted in the large-scale closed-loop wind tunnel at the Department of Energy and Process Engineering of the Norwegian University of Science and Technology (NTNU). The wind tunnel has a test-section with dimensions of 1.8 m $\times$ 2.71 m $\times$ 11.1 m in height, width and length, respectively. It houses a six-component force balance that can be rotated to vary the wing model's angle of attack and to obtain an accurate measure of the forces acting on it. Further details on the force balance measurements are given in § 2.3. The wind tunnel can also be fitted with an active turbulence grid 0.8 m from the start of the test section (after the tunnel's convergent section), which enables the generation of highly turbulent flows. The particular active grid used in this facility is described in detail by Kildal *et al.* (2023). It spans the entirety of the test section's cross-sectional area and consists of 90 shaft assemblies, with each assembly being individually operated by a dedicated integrated stepper motor. The mesh length of the grid is $M_g = 0.1$ m. The grid was operated with different 'fully random' (Hearst &

Lavoie 2015) sequences whereby the grid is sent top-hat distributions of the rotational velocity, rotation period and acceleration for each shaft individually. In this study, only the rotational velocity was varied between cases as this parameter was shown to have the greatest impact on the produced turbulence levels (Hearst & Lavoie 2015).

The employed finite-wing model was a rectangular, square-tipped half-wing with a NACA 4412 profile. It has a chord length of $c = 0.25$ m, a maximum thickness of $\tau = 0.03$ m and spans $b = 0.9$ m from the floor to the centre of the test-section. This profile was chosen because it is a commonly used reference geometry for which comparative measurements exist in the literature (Kay *et al.* 2020; Cruz Marquez *et al.* 2021*b*). The airfoil was machine-cut from a single block of polyurethane (Ebaboard 0600) which is an isotropic material with well-known characteristics and properties (flexural modulus of 900 ± 200 MPa). The airfoil was deliberately made of an isotropic material so that there is no preference for a particular loading. The airfoil was mounted vertically in the wind tunnel test-section and centred on the force balance. The leading-edge was 3 m ($= 30M_g = 12c$) downstream of the active grid as shown in the schematic in figure 1. The wing was rigidly mounted and clamped to the force balance at the root such that the rotation axis of the force balance passed through its midchord. This effectively made a pin joint, whereby the wing span and tip were free while the root was fixed. The mounting platform of the force balance was below the wind tunnel floor. Thus, only the NACA 4412 section was exposed to the flow and not the root or the clamping apparatus. Additionally, a 4 mm gap was left between the wind tunnel floor and the wing model so as to avoid contact, which might influence the force measurements.

The coordinate system used in this study, $[x, y, z]$, is as shown in the schematic in figure 1. The x-axis is along the streamwise direction, the y-axis along the transverse direction (width of the wind tunnel) and the z-axis along the wing's span (height of the wind tunnel). The corresponding velocity components are represented by $[u, v, w]$. The origin is at the wing's tip at the trailing edge when its angle of attack is $\alpha = 5°$, given that most of the results presented and discussed herein correspond to this wing configuration. A second coordinate system based on the wingtip vortex' centre will also be used herein, which is represented by $[\hat{y}, \hat{z}]$. In the rest of the document, $\overline{\cdot s}$ represents time-averaged quantities, $\cdot s'$ represents standard deviation, $\hat{\cdot s}$ represents time-averaged quantities in the $(\hat{y}, \hat{z})$ coordinate system, which are sometimes referred to as conditionally averaged quantities, and $\langle \cdot s \rangle$ represents azimuthal averaging.

2.2. *Test cases and incoming flow conditions*

The experiments were conducted at a mean freestream velocity of $U_\infty \approx 7.8\,\mathrm{m\,s^{-1}}$, corresponding to a chord-based Reynolds number $Re_c = U_\infty c/\nu = 1.4 \times 10^5$. This is within the range of Reynolds numbers investigated in previous studies (see table 1) and was selected because it was the minimum velocity whereby Reynolds number independence was observed.

Four turbulent flow conditions were generated and investigated for this study: REF, A, B and C. The first test condition, REF, was a low turbulence reference case without the active grid. For case A, the active grid was in place but kept static and fully open, producing a turbulent flow with low intensity. For the last two cases, the active grid was actuated in two modes to generate approximately homogeneous, isotropic turbulence. Case B involved spinning all the vertical axes of the active grid at a frequency of 7 ± 2 Hz, while in the last case (C), both the horizontal and vertical axes were spun at a frequency of 5 ± 2 Hz.

A preliminary study using HWA was carried out to characterise the incoming flow conditions corresponding to the four test cases and to ascertain flow homogeneity in

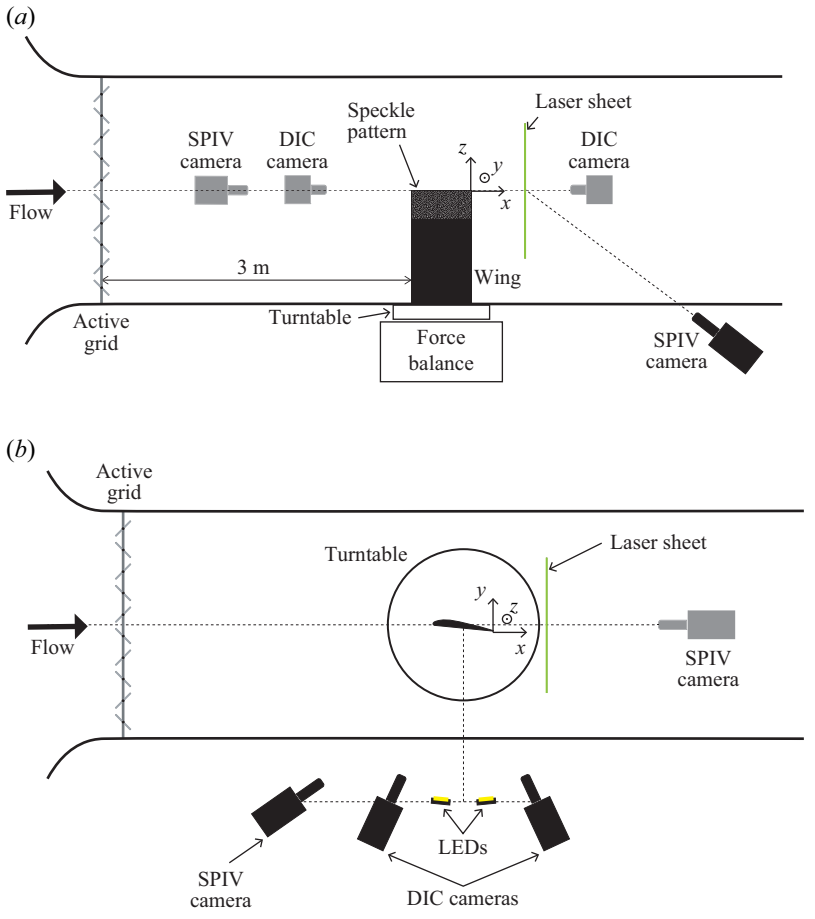

Figure 1. Schematics of the experimental set-up (not to scale), showing the wind tunnel, active grid, flexible wing model with speckle pattern, turntable, force balance and the digital image correlation (DIC) and stereoscopic particle image velocimetry (SPIV) systems (including cameras, laser sheet and light-emitting-diode (LED) illumination). The coordinate system is also indicated. (*a*) Side view of the wind tunnel's central plane (grey cameras were mounted on the tunnel's side); (*b*) top view (grey SPIV camera located beneath the tunnel).

the wind tunnel test section without the wing. A Dantec 55P11 single hot-wire probe, controlled by a Dantec StreamLine Pro constant temperature anemometer, was employed. The probe was fixed in close proximity to a Pitot-static tube during all the tests. This system was fixed to a four degree-of-freedom wind tunnel traverse in order to measure the incoming flow at different locations in the wind tunnel. A thermocouple was used to measure the flow temperature. The hot-wire signals were sampled at a nominal acquisition rate of 75 kHz, with an analogue low-pass cutoff filter set to 30 kHz. Before and after each test case, the hot-wire probe was calibrated against the Pitot-static tube at the wind tunnel's centreline, $80M_g$ downstream of the active grid. The calibration was performed for 11 velocities (from 2.3 to 15.5 m s^{-1}). The temperature correction methodology of Hultmark & Smits (2010) was employed. During postprocessing, a seventh-order low-pass Butterworth filter was applied to the time series at $1.1f_\eta$, where f_η is the Kolmogorov advection frequency.

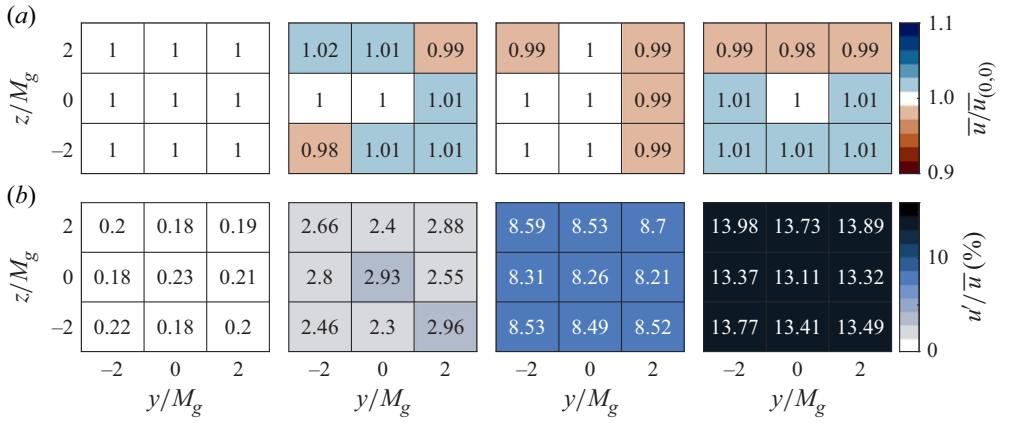

Figure 2. Homogeneity of the flow in a $4M_g \times 4M_g$ array $30M_g$ downstream of the active grid. The values for $\overline{u}$ (*a*) are normalised by the respective centreline velocity $\overline{u}_{(0,0)}$. The values for $u'/\overline{u}$ (*b*) are the turbulence intensities as a percentage.

To assess the flow characteristics in the wind tunnel for the four test cases, the base flows without the wing were evaluated along the centreline of the wind tunnel from $0.8c$ upstream of the leading edge of the wing to $2.2c$ downstream of the trailing edge in steps of $2M_g$, as well as in a plane consisting of 3×3 points situated at the leading edge. For these tests, hot-wire samples for cases A, B and C were acquired for 120 s; data were only acquired for 30 s for the REF case as this flow was nearly laminar. Specifically at $30M_g$ downstream of the active grid (the wing's leading edge), data were acquired for 600 s for cases A, B and C, and 120 s for case REF, respectively, to converge the turbulent spectra. The mean velocity remained relatively constant for all test conditions, with standard deviations from the average value of the mean velocities along the centreline of 0.8 % for the worst case. The streamwise scan showed that the turbulence intensity ($u'/\overline{u}$) remained around 0.2 % for REF, decayed from 3 % to 2.5 % for A, from 8.5 % to 7.8 % for B, and from 13 % to 11.5 % for C. Such a result is expected as grid-generated turbulence decays in space in a wind tunnel (see, for example, Comte-Bellot & Corrsin 1966) and is reported here only for completeness.

A measure of the homogeneity of the flow along the transverse direction (y–z plane) was obtained by conducting planar scans at $30M_g$ downstream of the active grid (the leading edge of the wing) were performed over a $4M_g \times 4M_g$ grid oriented perpendicular to the flow. The analysis array consisted of nine points, with the central point being the second point used in the centreline homogeneity analysis reported previously. The homogeneity in the mean and fluctuating velocity components of the flow over the $4M_g \times 4M_g$ array is shown in figure 2. The cases generally show homogeneity of the mean velocity within ± 2 % of the centreline velocity and reasonable uniformity of the turbulence intensity.

The turbulence properties of the incoming flow measured at a distance of $30M_g$ downstream of the inlet on the centreline for the four test cases are summarised in table 2. The table includes values for the turbulence intensity $u'/\overline{u}$, the integral length scale L_{uu} obtained from integrating the autocorrelation function of the velocity fluctuations to the first zero-crossing, the Taylor-microscale-based Reynolds number $Re_\lambda = \lambda_T u'/\nu$ and the global isotropy ratio. The square of the Taylor microscale is given by $\lambda_T^2 = u'^2/\langle(\partial u'/\partial x)^2\rangle$ and was calculated by estimating the gradients using Taylor's hypothesis and a seventh-order centred-difference scheme as described in Hearst *et al.* (2012). Using the method described by Benedict & Gould (1996), the maximum random error in the turbulence

Inflow case	$\Omega \pm \omega$ (Hz)		$u'/\overline{u}$ (%)	L_{uu}/c	Re_λ	$u'/\frac{1}{2}(v'+w')$
REF	—	(no grid)	0.23	—	—	1.15
A	—	(static)	2.93	0.13	77	1.34
B	7 ± 2	(vertical)	8.26	0.58	300	1.15
C	5 ± 2	(all)	13.11	0.71	429	1.04

Table 2. Summary of the turbulence properties in the wind tunnel without the wing. Statistics are for $30M_g$ downstream of the active grid along the centreline ($(y, z) = (0, 0)$ in figure 2, wing's leading edge), except for the isotropy ratios which were computed from PIV in the empty tunnel at the same location as the SPIV measurements for the wingtip vortex analysis, i.e. $37.5M_g$ from the grid or $2c$ downstream of the airfoil trailing edge.

intensity measurement was determined to be approximately 1.5 %. The global isotropy ratio was measured by spatially averaging the isotropy ratio over the SPIV field-of-view (FOV) (described in § 2.4) acquired at $37.5M_g$ without the wing model present. Here, the transverse velocity components are averaged when put in the global isotropy ratio to create a single parameter. The isotropy ratio approaches unity as the turbulence level of the active grid is increased; note REF is not acquired with the active grid and thus does not follow the aforementioned trend and instead illustrates the background isotropy in the empty facility.

The cases reported in table 2 illustrate that the FST intensity and Re_λ increase from case REF to case C; however, so does the integral length scale. As such, when the FST is described as 'increasing,' this should be understood to mean that the scale of the turbulence is increasing, i.e. it is both more energetic and contains energy at larger length scales.

The turbulent velocity spectra obtained from the hot-wire measurements for all cases are shown in figure 3. When viscous unit normalisation is used (figure 3*b*), all turbulent spectra collapse at the small scales and differ only at the large scales, as one expects. A $\kappa^{-5/3}$ line (black dashed) is added for reference. The absence of low-frequency peaks in the spectra indicates that the active grid forcing does not preferentially energise a particular frequency or set of frequencies, which is a desired outcome. As the turbulence intensity increases, the inertial range grows as expected from previous active grid measurements (Larssen & Devenport 2011; Hearst & Lavoie 2015) and turbulence theory for increasing Re_λ.

2.3. *Force measurements*

The different forces acting on the wing model at various test conditions were measured using the six-component force balance that is housed in the wind tunnel. Before conducting force measurements, load cell calibration was performed using known standard reference weights. Offset measurements were taken before and after each set of measurements to monitor and account for any sensor drift. Linear interpolation was carried out to compensate for any drift. Force measurements were acquired for angles of attack in the range $-5° \leqslant \alpha \leqslant +26°$. Data acquisition was performed at a sampling frequency of 2 kHz for each angle of attack. For cases REF and A, one 240 s sample was acquired for each α. In order to obtain converged results for the two most turbulent cases, B and C, 540 s of data were acquired at each α; these data were acquired as three independent 180 s samples. By propagating the following sources of uncertainty – an assumed angle-of-attack uncertainty of 0.5° and the residual square errors from the calibration – the maximum uncertainty in the measured lift force is estimated to be approximately 0.67 N, which corresponds to a relative uncertainty of approximately 5.7 % – 9.5 %.

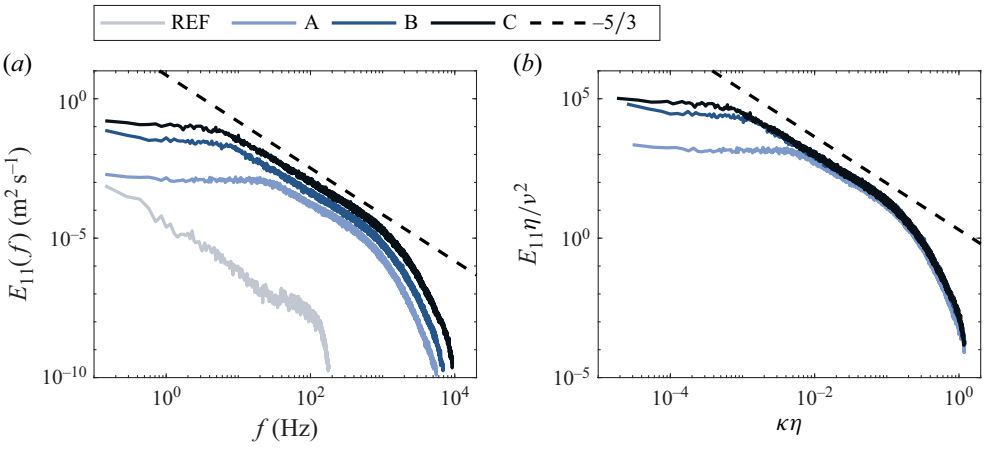

Figure 3. Velocity spectra for all cases plotted in (*a*) dimensional frequency-space and (*b*) wavenumber-space normalised with viscous units. The REF case is only plotted in (*a*) because its turbulence level is too low to be meaningfully represented by the normalisation in (*b*).

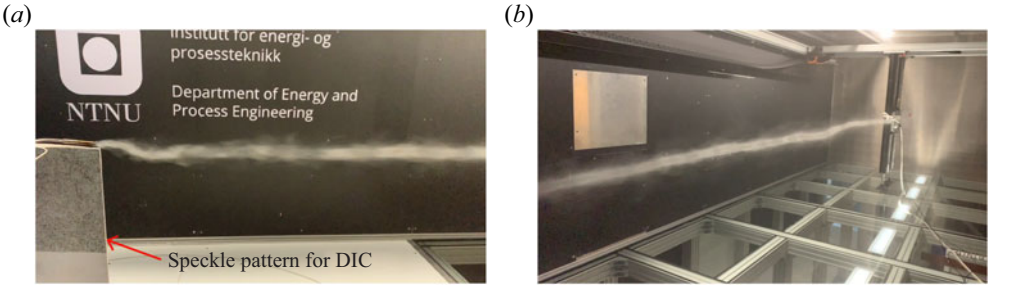

Figure 4. Smoke visualisation of the wingtip vortex (*a*) near the trailing edge, and (*b*) downstream up to approximately 30 c. The flow case is C in these images and the velocity was reduced to decrease the dispersion of the smoke plume.

2.4. *Stereoscopic particle image velocimetry measurements*

Cross-stream SPIV was employed to measure the three components of the instantaneous velocity field in the wake of the wing. The FOV is in the yz-plane. During these measurements, the wing was maintained at an angle of attack of $\alpha = 5°$. A preliminary smoke visualisation exercise was carried out at the four incoming turbulence conditions to estimate the tip vortex' location, in order to place the SPIV system. Figures 4(*a*) and 4(*b*) show the evolution of the wingtip vortex downstream of the trailing edge for case C (the most turbulent case) at low velocity; low velocity was used to facilitate the qualitative visualisation. Based on this, the streamwise station 2c downstream of the wing's trailing edge was chosen for the SPIV measurements as the vortex tended to remain within the plausible particle image velocimetry (PIV) measurement domain and there are reference measurements from previous experimental studies (Serrano-Aguilera *et al.* 2016; Bölle *et al.* 2023). The imaging set-up is shown in figure 1.

The air flow was seeded with di-ethyl-hexyl-sebacate particles of approximately 1 µm diameter. The particles were illuminated with a Litron LDY303HE dual-pulse Nd:YLF laser emitting green light at a wavelength of 527 nm. The laser head was placed outside the wind tunnel. Using an appropriate set of laser optics, the beam was shaped into a

≈1 mm-thick sheet, which entered the test section from the side through the available optical axis.

Imaging was carried out using two high-speed Phantom v2012 1 MP cameras featuring a $1280 \times 800\ \text{px}^2$ complementary metal-oxide-semiconductor (CMOS) sensor (28 μm pixel pitch, 12 bits of digital resolution). These cameras were equipped with Nikon Nikkor 200 mm macrolenses operated at $f_\# = 5.6$. Green filters were attached to the lenses to reduce the effect of other wavelengths (particularly from the LEDs used for DIC, see § 2.5) and improve the signal-to-noise ratio of the acquired SPIV images. The first camera was located on the side of the wind tunnel and directed towards the upstream side of the measured FOV, while the second camera was placed along the centreline ($y = 0$) beneath the wind tunnel, downstream of the wing. In order to coincide with the measurement plane and to ensure that both cameras capture sharp and in-focus images of the particles in the same plane, Scheimpflug adapters were used to tilt the focal plane of each camera.

The laser, the two SPIV cameras and the two cameras used for DIC (described in § 2.5) were synchronised using a LaVision PTU X controller and the Davis 10.2 software suite. Images were captured in double-frame mode, with a pulse separation of 95 μs between an image pair. For each test case, 10 000 image pairs were captured at a rate of 200 Hz, leading to a total sampling time of 50 s. Image preprocessing, calibration and vector computations were also carried out using Davis 10.2. Calibration was done using a LaVision Type 20 two-level calibration plate. Cross-correlation for vector field computation was carried out using multiple passes with a final interrogation window of 32 px × 32 px and a relative overlap of 50 %, resulting in a vector spacing of approximately 3 mm in both the y and z directions. The final field was cropped to 54 × 54 vectors (160 mm × 160 mm) near the centre of the FOV where the vector quality was high.

Measurement uncertainties are quantified for the REF case. The estimated errors in the instantaneous in-plane velocity components (v, w) are approximately $0.2\ \text{m s}^{-1}$, while the out-of-plane velocity component (u) has an estimated error of $0.4\ \text{m s}^{-1}$. Given a freestream velocity of $7.8\ \text{m s}^{-1}$, these correspond to relative uncertainties of approximately 2.6 % and 5.1 %, respectively. Using the linear error propagation technique summarised by Sciacchitano & Wieneke (2016), the uncertainty of the mean velocity for the out-of-plane component (which has the highest uncertainty) was ±0.4, 0.9, 0.9 and 1.2 % for cases REF, A, B and C, respectively.

2.5. *Digital image correlation measurements*

Digital image correlation is an optical method that enables non-contact measurement of surface deformation and displacement. To this effect, a speckle pattern was applied on the wing, which can be seen in figure 4(*a*). The speckle pattern consisted of randomly arranged points, each approximately 0.5 mm in diameter. Images of this pattern were acquired with no load to get the reference position. Then images were captured simultaneously with the PIV measurements to get a time series of the displacement and deformation. The experimental set-up used for the DIC is shown in figure 1. Imaging was carried out using two Photron SA 1.1 cameras featuring a 1024 px × 1024 px monochrome CMOS sensor (20 μm pixel pitch, 12 bits of digital resolution). They were positioned on the side of the wind tunnel and imaged the pressure side of the airfoil. The cameras were equipped with Sigma 50−100 mm lenses, which were adjusted to a numerical aperture of $f_\# = 1.8$, and had a focal length of 100 mm. This resulted in a scaling of $\approx 0.3\ \text{mm px}^{-1}$. The selected FOV was a rectangular area of 53.7 mm × 218.4 mm in height and width, respectively, located at the tip of the wing. Note that the full sensor of the camera was not used. To achieve uniform illumination across the wing's surface-of-interest, the set-up incorporated

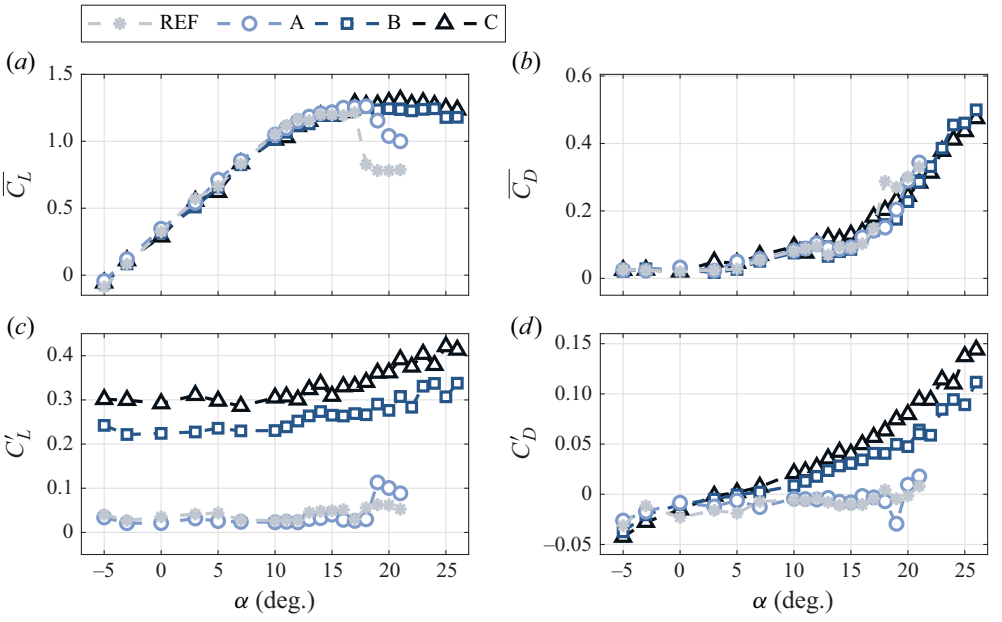

Figure 5. Impact of FST on the time-averaged (*a*) lift and (*b*) drag of the NACA 4412 flexible finite wing. The standard deviation of the (*c*) lift and (*d*) drag measurements that represent the fluctuations in the measured forces is also presented.

two GS Vitec LED light sources positioned between the two DIC cameras as shown in figure 1. Polarisers were used on both the LEDs and cameras to reduce glare. Finally, given the simultaneous operation of the SPIV and DIC systems, a 200 μs delay was added to the DIC system to minimise the green laser's interference with the DIC measurements.

Stereoscopic image calibration for DIC was done using a calibration cylinder with a reference pattern. A global DIC approach was employed to extract displacement information from the recorded images. A mesh with Q4 elements and an element size of 15 data points was used during processing. Bicubic spline interpolation and grey level normalisation were also employed. Images acquired during the REF case where the wing's deformations were negligible (discussed in § 3.2) were used to quantify the noise level in the deformation measurements. The noise level was taken as the standard deviation of the deflections (y-direction deformations) over the entire FOV and averaged over 10 images. It was found to be 0.005 mm.

3. Effect of FST on the wing

3.1. *Forces on the wing*

To understand how the finite-wing as a whole behaves in the produced turbulent flows, force balance measurements as introduced in § 2.3 were performed for $-5° \leqslant \alpha \leqslant +26°$. As is typical of airfoil measurements, hysteresis was observed when comparing results for increasing and decreasing α over the same range. As such, all results presented herein are for increasing α. Figure 5(*a*) shows the variation of the time-averaged three-dimensional (3-D) lift coefficient with angle of attack for the four test cases. The 3-D lift coefficient is expressed as $C_L = L/((1/2)\rho U_\infty^2 A)$, where L is the lift force measured by the force balance, ρ is the air density and A is the reference surface area of the wing. In the present results, slopes of the lift curves are approximately collapsed within the uncertainty of the

	Leading edge				Trailing edge			
	REF	A	B	C	REF	A	B	C
$\overline{\Delta y_w}/\tau$ (%)	0.04	0.16	4.48	12.51	0.05	0.11	4.58	13.00
$\Delta y_w'/\tau$ (%)	0.05	0.12	5.38	7.09	0.06	0.12	5.53	7.25

Table 3. Mean of the wing's (absolute) deflections and its standard deviation along the lift direction (Δy_w) at the leading and trailing edges non-dimensionalised with the maximum thickness of the wing, τ.

measurement for the linear range. This suggests that FST has little influence on the mean aerodynamic behaviour of the finite wing in this region and is in line with the observations of Wang *et al.* (2014). A slight increase in the maximum lift coefficient is observed when increasing turbulence intensity. This is consistent with the works of Li & Hearst (2021) and Thompson *et al.* (2023) but in opposition with the findings of Kay *et al.* (2020), who observed a decrease in the maximum 2-D lift coefficient of a NACA 4412 airfoil when increasing the FST intensity from 1.3 % to 15 %.

From $\alpha = 15°$, the lift curves are no longer collapsed in the current measurements. At lower levels of turbulence, the wing exhibited traditional stall behaviour characterised by a sharp drop in lift between $\alpha = 17°$ and 18°. On the drag coefficient curve, $C_D = D/((1/2)\rho U_\infty^2 A)$ (where D is the drag), for the low turbulent case shown in figure 5(*b*), this resulted in a sudden increase in drag. As the FST intensity was increased, the angle at which stall occurred shifted to larger α. This finding is consistent with several previous studies (Swalwell, Sheridan & Melbourne 2001; Ahmadi-Baloutaki *et al.* 2014; Kay *et al.* 2020; Thompson *et al.* 2023). The delay in stall with the addition of FST is likely a result of the boundary layer remaining attached at higher α and the suppression of the recirculation region, as demonstrated for similar FST conditions by Thompson *et al.* (2023, 2025). Furthermore, no sudden stall was observed. Instead, the wing gradually lost lift while the drag increased up to $\alpha = 26°$.

Finally, to account for the fluctuations caused by the turbulence, the standard deviation of the lift and drag time series are shown in figures 5(*c*) and 5(*d*). These fluctuations increase with FST intensity in agreement with the findings of Thompson *et al.* (2023). The observed increase in fluctuations suggests that FST has an impact on the instantaneous lift coefficient. Additionally, the drag curve displays a progressively increasing sensitivity to turbulence as α increases, with minimal fluctuations observed when approaching $\alpha = 0°$.

3.2. *Wing deflections*

In this section, the analysis of the wingtip displacements caused by the different turbulence cases measured with DIC (introduced in § 2.5) is presented. The statistical parameters, namely the mean and standard deviation of the deflections normalised with the wing's maximum thickness, τ, characterising the wing's deflection along the lift direction (Δy_w) are presented in table 3. The maximum mean deflection of the wing is 12 %−13 % while the maximum standard deviation of this parameter is ≈7 %. When normalised with the wing's span instead of thickness, the mean and standard deviation of the deflections are $\lesssim$1 %. Thus, the current wing model is certainly flexible, but far from the traditional ascription of the term aeroelastic. The mean of the wing's (absolute) deflections and the corresponding standard deviations are seen to increase with FST. This indicates that the deflections are both greater and more violent as one increases the turbulence intensity.

Singular value decomposition (SVD) was applied on the fluctuating component of the DIC measurements to study the wing's deformation in more detail, the results pertaining

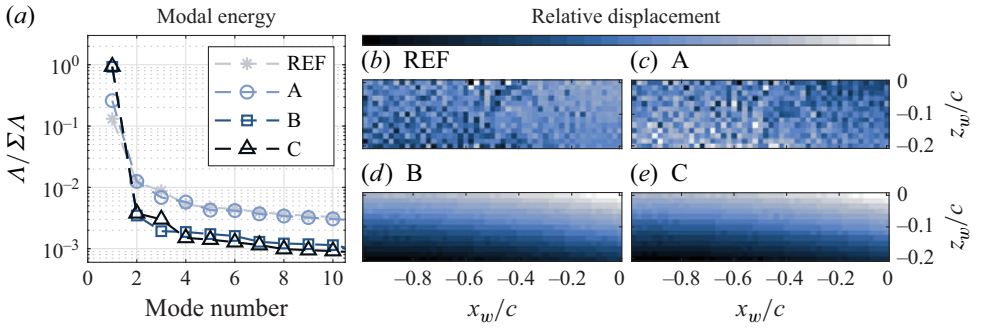

Figure 6. SVD of DIC measurements. The relative energy of the various modes compared with the total energy for the different cases is presented in (*a*). Spatial eigenfunction of the most energetic SVD mode of the different cases are shown in (*b–d*).

to which are presented in figure 6. The first SVD mode contains 13.2 %, 26 %, 92.5 % and 93.5 % of the total energy for cases REF, A, B and C, respectively, as shown in figure 6(*a*). These are the most energetic modes of the respective cases, with the second modes containing only ≈1 % of the total energy.

The spatial organisation of the fluctuations corresponding to the most energetic mode for each tested case are presented in figure 6(*b–e*). Here, a coordinate system specific to the wing model (x_w, y_w, z_w) is used. While z_w is aligned with the z direction of the main coordinate system, x_w and y_w are marginally different from the x and y coordinate owing to the $\alpha = 5°$ angle of the wing. The colour scale used here reflects relative values rather than absolutes, as the focus here is on the relative displacements of the wingtip points with respect to each other. These most energetic modes identify that the wingtip primarily bends along the lift direction (i.e. $\pm y$). Thus, the wing exhibits the behaviour of a cantilever beam. For cases REF and A, this mode is not particularly strong, while for cases B and C it is quite clear that the airfoil bends off at the tip. While it is not shown here, the second SVD modes corresponded to the twisting motion of the wing along its midchord. However, as previously stated, this mode contained an order-of-magnitude less energy than the first mode. This response of the wing's structure is similar to the flexible wing experiments of Chen *et al.* (2018*b*) and Thompson *et al.* (2025), where the bending deformation of the wingtip was shown to be much stronger than the torsional deformation with the addition of incoming fluctuations. Similar to the observations from the statistical analysis in table 3, SVD computations also indicate that the wing's vibration increases with incoming FST. However, it seems to have a significant effect only on the bending motion of the wing and does not influence the wing's twist along its midchord.

The frequency spectra of the displacement of the wingtip trailing edge are presented in figure 7(*a*). The natural frequency of the wing's structure was measured in a static (no flow) environment by striking the airfoil and measuring its response with a laser displacement sensor (ILD2310-05) and was found to be 6.2 Hz. In all turbulence cases, a distinct energy peak is observed at the same frequency, which corresponds to a chord-based reduced frequency of $fc/U_\infty = 0.2$. It is worth noting that while it is not presented here, the frequency content of the first SVD mode also corresponds to the same value. Thus, the magnitude of the wing's vibration is sensitive to the level of incoming turbulence, but the specific active frequency still remains the natural frequency of the wing.

Finally, as mentioned in § 3.1, the lift force measured using the force balance showed an increase in lift fluctuations with incoming turbulence intensity. This is especially apparent

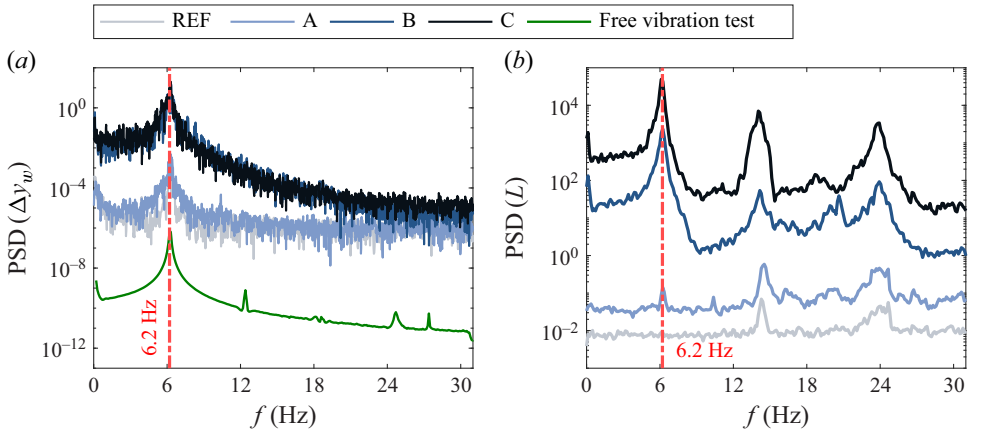

Figure 7. (*a*) Power spectra of the wingtip trailing edge displacement. The magnitude of the free vibration test spectrum was shifted vertically to ease comparison with the other spectra. (*b*) Power spectral density (PSD) computed on lift fluctuations measured using the force balance for $\alpha = 5°$. Spectra of cases A, B and C are shifted by 1, 2 and 3 decades, respectively, for clarity.

for cases B and C in figure 5(*c*). The spectra of these lift fluctuations when the wing is at $\alpha = 5°$ are presented in figure 7(*b*). The energy in the spectra of the cases REF and A are very low, which corroborates the observations in figure 5(*a*). Interestingly, however, for the high turbulence cases B and C, the dominant frequency in the lift fluctuations is observed to also be at 6.2 Hz. Thus, when the amplitude of the wing's vibration is high enough, the generated lift force is not constant any more, but fluctuates at the same frequency as the wing's vibrations.

4. Effect of FST on the wingtip vortex

4.1. *Swirling strength and vortex size*

The swirling strength (λ_{ci}), which is the imaginary part of the complex eigenvalue of the local velocity gradient tensor, is used to identify and depict the wingtip vortex. The contour maps of the time-averaged streamwise swirling strength, $\overline{\lambda}_{ci}$, for each test case are presented in figure 8(*a–d*). Here, the maximum swirling strength at the centre of the vortex was used to non-dimensionalise the rest of the field in order to maintain a consistent colour scale for all cases. The maximum values of the time-averaged swirling strength, normalised with global parameters, i.e. $\max(\overline{\lambda}_{ci}) \cdot c^2/U_\infty^2$, decreased with FST as shown in figure 8(*i*). In figure 8(*a–d*), a high concentration of swirling strength that is circular in shape is observed near the centre of the frame. The size of the swirling strength contours appear to grow with increasing FST. As highlighted in § 1, previous studies have demonstrated that an increase in the incoming turbulence intensity leads to an increase in the meandering amplitude of the wingtip vortex (Bailey & Tavoularis 2008; Pentelow 2014; Ben Miloud *et al.* 2020). In this context, the time-averaged swirling strength in figure 8(*a–d)* would naturally give the impression of a vortex that occupies more area. In reality, this figure does not provide information about the diffusion of the vortex, but is an indicator of how the FST increases vortex meandering.

To visualise and study the changes caused by the FST on the wingtip vortex itself, the swirling strength data was averaged across time after adjusting each instantaneous field to be such that the origin is at the vortex centre (i.e. the vortex-based coordinate system $(\hat{y}, \hat{z}) = (0, 0)$), following the data reduction method of Heyes *et al.* (2004).

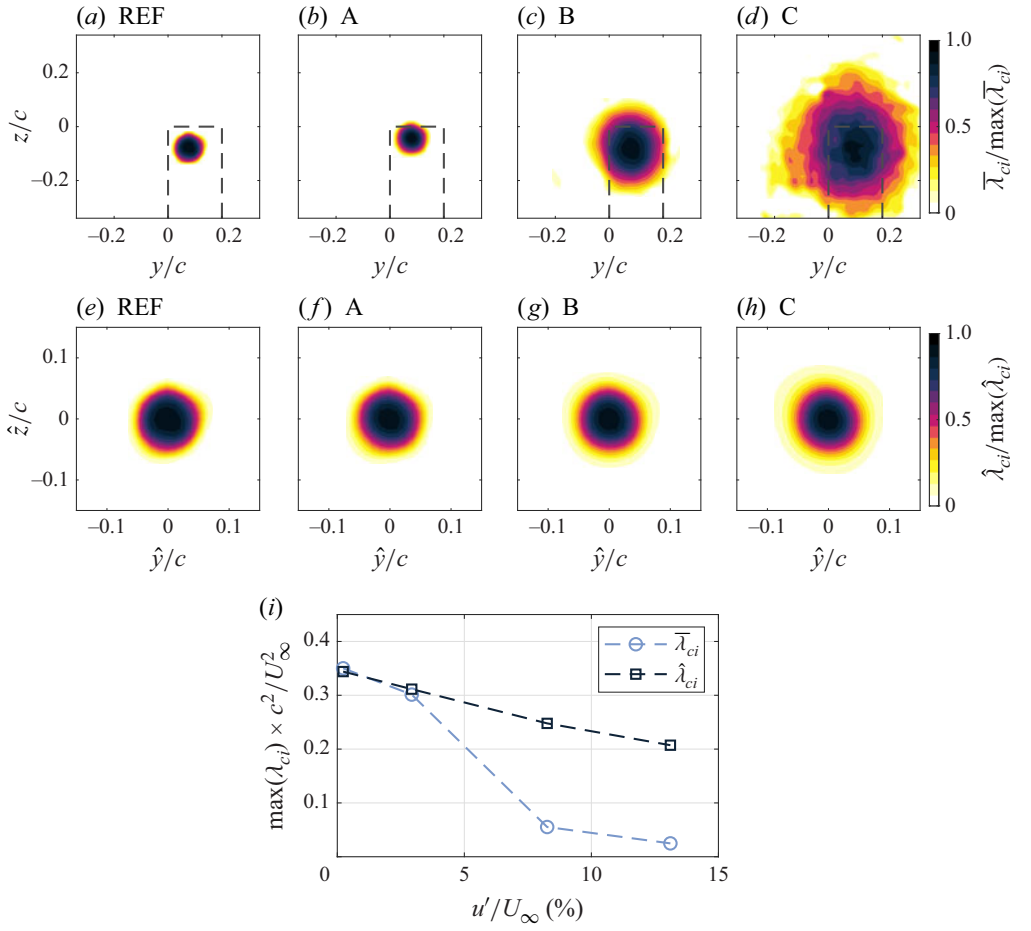

Figure 8. (*a–d*) Normalised global time-average of the swirling strength ($\overline{\lambda}_{ci}$) of the four test cases (no alignment of vortex-centres). The black dashed line represents the surface projection of the wing. (*e–h*) Normalised, conditionally time-averaged swirling strength ($\hat{\lambda}_{ci}$) of the four test cases (alignment of vortex centres). (*i*) Maxima of the time-averaged and conditionally time-averaged swirling strengths plotted against u'/U_∞. Note that the axes of (*e–h*) are smaller than (*a–d*).

This is henceforth referred to as conditional (time-)averaging (also introduced at end of § 2.1). To identify the centre of the vortex in each frame, a non-Galilean invariant approach introduced by Graftieaux, Michard & Grosjean (2001) was implemented. This approach consists of computing the Γ_1 criterion from the SPIV fields to extract the position of the vortex centre, with $\Gamma_1 \in [0, 1]$ defined as a scalar function,

$$\Gamma_1(P) = \frac{1}{N} \sum_S \frac{(\boldsymbol{R}_{PM} \times \boldsymbol{U}_M) \cdot \boldsymbol{e}_x}{|\boldsymbol{R}_{PM}|\,|\boldsymbol{U}_M|} = \frac{1}{N} \sum_S \sin(\theta_M), \tag{4.1}$$

where S is a 2-D area surrounding a fixed point defined by P, M is any point lying in S, $\boldsymbol{e}_x$ is the unit vector normal to the measurement plane and θ_M represents the angle between the velocity vector, $\boldsymbol{U}_M$, and the radius vector, $\boldsymbol{R}_{PM}$. When the angles θ_M between the velocity vectors at points M and the radius vector approach $\pi/2$ for a point P, Γ_1 tends towards unity, the maximum value for Γ_1. In practice, Γ_1 rarely reaches unity and the point of maximum Γ_1 is considered the vortex centre.

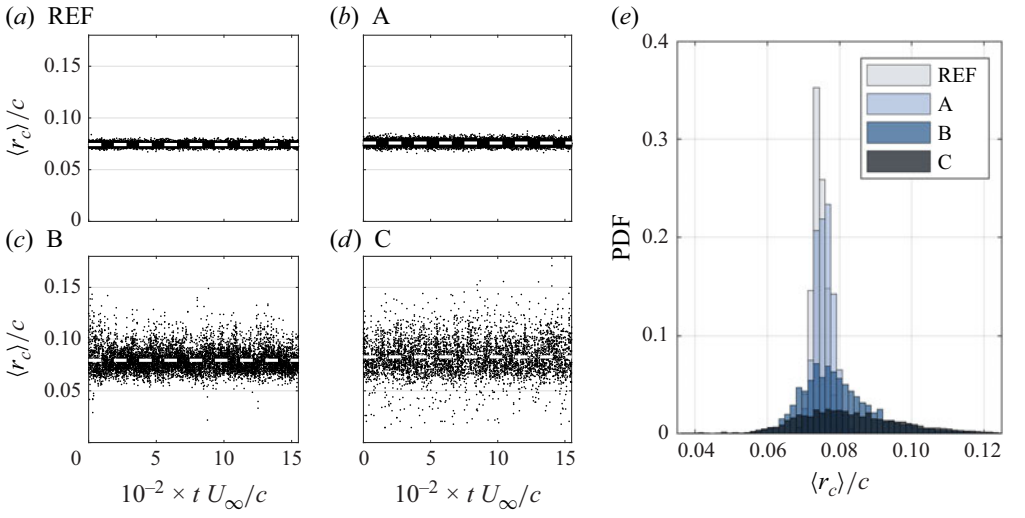

Figure 9. (*a-d*) Evolution of vortex core radius versus normalised time for the four test cases. Dashed (white) line represents mean radius. (*e*) Probability density function (PDF) of the vortex size.

The result of this procedure (i.e. determining the instantaneous vortex positions and recentring each swirl strength field before averaging across frames) is shown in figure 8(*e–h*). In these plots, the conditionally averaged swirl strength ($\hat{\lambda}_{ci}$) is normalised by the maximum value in the respective field. This normalisation highlights the relative distribution of swirling strength around the vortex core, which appears to broaden slightly with increasing FST, suggesting a slight diffusion of the vortex. Nonetheless, in this frame the change to the vortex is significantly smaller than the laboratory-frame averaging suggests. The corresponding maximum values of the conditionally averaged swirl strength for the different cases normalised with global parameters are presented in figure 8(*i*). A linear decrease of this parameter is observed with increasing FST, indicating a reduction in vortex strength, consistent with previous findings (Bailey *et al.* 2006; Ghimire & Bailey 2017; Ben Miloud *et al.* 2020).

The results in figure 8(*e–h*) indicate that the average vortex size remains fairly constant with FST. To investigate this further, figure 9(*a–d*) display the time evolution of the vortex-core radius, with the corresponding average value $r_c (= \langle \hat{r}_c \rangle)$ marked by dashed white lines. Herein, the vortex core radius is defined as the radial position of the maximum azimuthal velocity (see Appendix A). The vortex size remained relatively stable for cases REF and A. However, for case A, the deviation from the mean value increased, suggesting a slight decrease in the overall stability. For the more turbulent cases B and C, the deviation from the mean increases further, indicating larger changes to the size of the vortex in time. The average vortex radius, r_c, is shown through the PDF in figure 9(*d*), where a minor increase in average vortex size can be observed, with $r_c/c = 0.0743$ for case REF increasing to $r_c/c = 0.0828$ for case C. This is paired with an increase in scatter and a slight asymmetry in favour of larger vortices.

It is worth noting that azimuthal velocity profiles and the circulation within the tip vortex were also studied. These analyses are not included here for conciseness but can be found in Appendix A and are in good agreement with previous studies (Bailey *et al.* 2006; Pentelow 2014; Ghimire & Bailey 2017; Ben Miloud *et al.* 2020). Notably, the maximum azimuthal velocity within the vortex core decreases with increasing FST and it

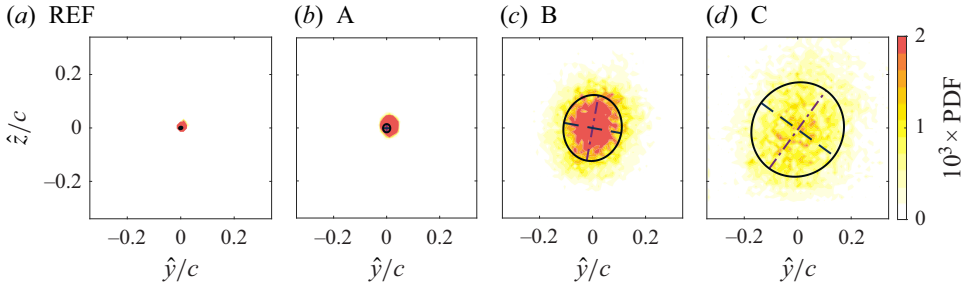

Figure 10. Probability density function of the instantaneous vortex centre relative to the mean vortex centre position (meandering conditioned) of the four different cases. A least-squares-based ellipse fit with its minor and major axis (dashed and dash–dotted, respectively) is also shown.

is also inferred that FST enhanced the rate at which the vortex reached its fully developed structure (Bailey *et al.* 2006; Ghimire & Bailey 2017). A possible reduction in circulation near the core radius indicating an increase in vortex diffusion with FST was also observed, which is in agreement with Ghimire & Bailey (2017) and Ben Miloud *et al.* (2020). This observation, in conjunction with a decrease in the maximum streamwise swirl strength (figure 8*i*) and a slight increase in the average radius of the tip vortex (figure 9), support the observation made with figure 8(*e–h*) that the diffusion of the vortex increases with FST.

4.2. *Probability distributions of vortex position and meandering amplitudes*

Bailey & Tavoularis (2008) and Van Jaarsveld *et al.* (2011) have previously reported that the meandering amplitude of the vortex, denoted in the current work by σ_i (i representing coordinate direction), increased with FST. Figure 10 presents the 2-D probability density distribution of the instantaneous vortex centres relative to its mean position. It is worth noting that it is this conditioned (fluctuations) signal that is used in the rest of this section when referring to vortex meandering. The darker colours in figure 10 represent the areas where the vortex centre was more likely to be located. For REF, the results show a highly localised vortex centre that remained stationary in time. For case A, the circular concentration area of the probability of the vortex centre location starts to extend, although it still remained fairly localised. In the two most turbulent cases (B and C), the PDFs indicate that the instantaneous vortex centre could be located in a wider area. Thus, as FST increased, there is a noticeable increase in the scattering of the vortex positions, in agreement with Bailey & Tavoularis (2008) and Van Jaarsveld *et al.* (2011), indicating an increase in vortex meandering.

To determine the meandering amplitudes in the transverse and vertical directions, denoted by σ_y and σ_z, respectively, the standard deviations of the time series for the vortex axis displacements from the mean position were calculated for each direction. The dependence of these amplitudes on the incoming turbulence intensity is presented in figure 11. As expected and noted by Bailey *et al.* (2018) and Ben Miloud *et al.* (2020), the meandering amplitudes strongly increase in both directions with FST. While previous efforts demonstrated this only for turbulence intensities less than 6 %, the current results show that this tendency remains true even at the highest tested turbulence intensity of 13 %. Furthermore, the meandering is homogeneous in both directions of the transverse plane.

Finally, ellipses were fitted to the vortex-position data using a least-squares method, and are plotted on the PDFs in figure 10. For this fit, only the data points where the tip vortex was within the region defined by $\hat{y}/c = \pm\sigma_y \cdot \sqrt{2}$ and $\hat{z}/c = \pm\sigma_z \cdot \sqrt{2}$ were considered.

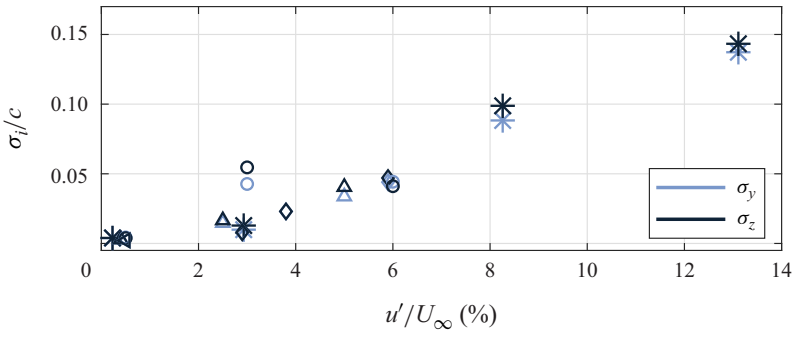

Figure 11. Variation of meandering amplitude (σ_i) with incoming turbulence intensity: $*$, present results; $\triangle$, Bailey & Tavoularis (2008) ($x/c = 3$, $Re_c = 2.4 \times 10^5$); $\Diamond$, Pentelow (2014) ($x/c = 2.85$, $Re_c = 2.4 \times 10^4$); $\circ$, Ben Miloud *et al.* (2020) ($x/c = 2.5$, $Re_c = 2.0 \times 10^5$); $\triangleleft$, Bölle *et al.* (2023) ($x/c = 2$, $Re_c = 1.7 \times 10^5$).

The ratio of the major and minor axes of the ellipse was $\approx$1.1 for all cases, which suggests that the meandering motion was approximately homogeneous in the transverse plane. The orientation or tilt of the ellipse, however, increased with FST. It was negligible for case A but increased to 0.06π and 0.2π for cases B and C, respectively. This is an indication that the meandering tends in the direction of the lift force with increasing FST intensity. In the flexible wing experiments of Chen *et al.* (2018*b*), probability distribution of the instantaneous vortex location was more dispersed downstream of the flexible wing compared with their rigid wing. This suggests that the current observations may be attributed to the wing's deflections, a point that will be explored further in § 5.

4.3. *Spectral signature of wingtip-vortex' motion*

The frequency content of the vortex core's motion is investigated further, to complement the results of the meandering amplitude. Given that the dominant vibration of the wing is along the lift (i.e. y) direction as shown in § 3.2, only the meandering spectra associated with the transverse direction, $\phi_{yy}(f)$, are presented and discussed further.

The premultiplied frequency spectra of the vortex motion for each turbulent case, as presented in the literature (see Bailey *et al.* 2018; Chen *et al.* 2018*a*) are shown in figure 12. The vertical (red) dash–dotted lines correspond to the wing's vibration frequency (6.2 Hz) in normalised form. Note that, in some frames, the identification of the vortex centre using the Γ_1 criterion was not conclusive; often because, for the higher turbulence conditions, the vortex moved out of SPIV FOV for short periods. Consequently, the amount of information lost in these cases was 0 %, 0 %, $\approx$1 % and $\approx$10 % for cases REF, A, B and C, respectively. The fillgaps () function in MATLAB, which estimates the missing values through forward and backward autoregressive fits of the remaining data, was employed to fill the missing data. This was validated by taking complete sections of the data and removing data points and refilling them with this approach; the statistics and spectra were found to be preserved.

Figure 10 demonstrates that vortex meandering motion for the REF case is minimal. Thus, the spectrum in figure 12(*a*) shows no specific dominant frequency. With the addition of FST (figure 12*b–d*), the meandering energy is seen to be in a frequency band spread over two orders-of-magnitude. Between the least (A) and most turbulent (C) cases, the energy under the curve has a difference of two orders-of-magnitude. These observations are consistent with the results shown earlier regarding vortex position in the $y-z$ plane (figure 10) and the amplitude of meandering (figure 11).

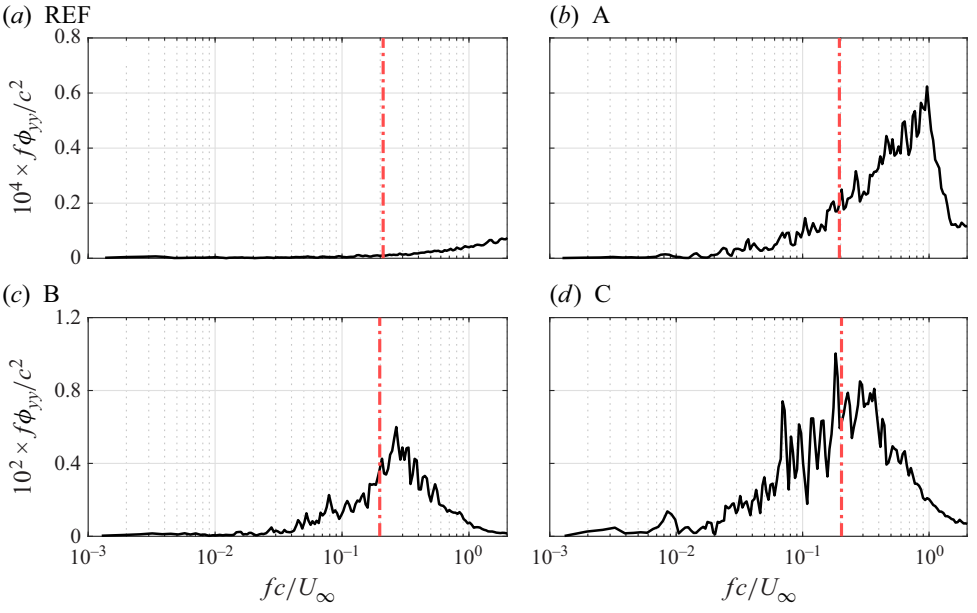

Figure 12. Premultiplied frequency spectra of the vortex motion ϕ_{yy}. Dash–dotted (red) line indicates normalised frequency of the wing's vibration. Note that the vertical axes of (*a*) and (*b*) are two orders-of-magnitude lower than (*c*) and (*d*).

The broadband nature of the meandering spectra centred around some frequency band was shown also by Bailey *et al.* (2018). This demonstrates the stochastic nature of tip-vortex meandering and that the measured meandering is composed of displacements at different scales. The fluctuations in this broad frequency band correspond to relatively long wavelengths ($\lambda = U_\infty/f$) in the range $0.74 < \lambda/c < 83$ ($10 < \lambda/r_c < 1000$). It has been shown previously that even in low turbulence conditions ($u'/U_\infty \approx 0.5\,\%$), the long wavelength motions are more dominant than short wavelengths (Chen *et al.* 2018*a*). Furthermore, based on the observations of Bailey *et al.* (2018), the addition of FST mostly dampens short-wavelength motions. Considering both these observations in the previous literature, the short-wavelength vortex motion is not expected to be dominant in the current results either.

Together with the energy within the frequency band associated with vortex motion increasing, a reduction in the peak frequency (both normalised and dimensional) is also seen in figure 12(*b–d*). One can thus identify that the strongest vortex motion occurs at lower frequencies (or larger meandering wavelengths) as the intensity of incoming turbulence increases. A similar observation was made by Bailey *et al.* (2018) when comparing their low-turbulence case and high-turbulence cases in the near wake. However, the current set-up includes a flexible wing which could have additional effects on the vortex dynamics on top of the incoming turbulence.

Artefacts of the wing's vibrations are noticeable in the spectra of all cases with the active grid. In case A (figure 12*b*), a small peak is noticed at the normalised frequency of 0.2 which could be attributed to the vibration of the wing, but it is an order-of-magnitude lower in energy compared with the peak in the spectrum. A similar observation can be made in figure 12(*c*) showing the spectrum of case B. The spectral peak at the normalised frequency of the wing's vibration is now close to the maxima of the frequency band. In the most turbulent case C in figure 12(*d*), the wing's vibration frequency is within the

dominant vortex motion's frequency range. Thus, these results strongly suggest that the spectral content of the vortex core's displacement is linked to the frequency of the wingtip motion.

4.4. *Proper orthogonal decomposition assessment of vortex meandering*

More insight into the dynamics of wingtip vortices can be obtained using POD (see, for example, Edstrand *et al.* 2016, Chen *et al.* 2018*a*,*b* and Dghim *et al.* 2021). The same is done here to further investigate the impact of FST on the wingtip vortex. The snapshot formulation of POD proposed by Sirovich (1987) is employed for this purpose. It was applied only on the fluctuation fields of the transverse velocity components. In doing so, the fluctuating velocity fields arranged in matrix form as $Q = [(v - \overline{v}); (w - \overline{w})]$ are decomposed in the following manner:

$$Q(y, z, t) = \sum_n \Lambda_n \Theta_n(t) \Psi_n(y, z). \tag{4.2}$$

Here, $\Psi_n(y, z)$ are a set of empirical eigenfunctions (spatial POD modes) that contain information regarding the spatial organisation of various fluctuations with corresponding eigenvalues, Λ_n, representing the modal energy and temporal coefficients, $\Theta_n(t)$, with n being the mode number. It is worth noting that the modes are sorted in descending order of their relative modal energy. Henceforth, any mention of mode number corresponds to its rank based on its relative modal energy. Furthermore, given that the amplitude of meandering was very low for the REF case (figure 11) and that the frequency content of the vortex' motion in this flow condition is not well resolved in the current data as seen in figure 12(*a*), it is not considered in the current analysis. The first four spatial modes (y component) of cases A, B and C are shown in figure 13 as filled contours. The cross product of the two components of the POD spatial modes, which can be related to vorticity along the streamwise direction ($\Omega_n^x = \nabla \times \Psi_n(y, z)$), is computed and also shown in these plots as green and pink contour lines. The relative modal energy of the first 10 eigenmodes is presented in figure 14(*a*). The spectra of the temporal coefficients of the first four POD modes are plotted in figure 14(*b–d*) for cases A, B and C, respectively.

When looking at the Ω_n^x contour lines in figure 13, the first modes of all three cases contain two regions of oppositely signed vorticity, forming a vortex dipole together. A similar organisation of fluctuations is observed in the second mode of cases A and B as well. In case C (figure 13*f*), while there are two structures observed, the shape of the one on the right-hand side is not as well-resolved as the rest. Nevertheless, these appear to be paired in all three cases and orthogonally rotate together. As such, these mode-pairs could be associated with helical displacement modes arising from a Kelvin wave with an azimuthal wavenumber of $m = 1$ as was conjectured by previous studies as well (Fabre, Sipp & Jacquin 2006; Dghim *et al.* 2021). A deeper analysis of the vortex stability would be useful to confirm this in the future. Nevertheless, this dipole is a result of the transverse velocity components being non-zero at its centre, which leads to vortex meandering (Fabre *et al.* 2006; Edstrand *et al.* 2016; Chen *et al.* 2018*a*,*b*; Dghim *et al.* 2021). This last idea is in fact supported by the POD results presented here. The filled contours in figure 13(*a–f*), which represent the organisation of transverse velocity fluctuations in the y direction ($\Psi_n^y(y, z)$), is non-zero at the centre of the dipole in the first two modes of all three cases.

The structures in these spatial modes also increase in size with FST, which is synonymous with the increase in the size of the swirl-strength contour in figures 8(*a–d*). The relative energies of these mode-pairs also increase with the addition of turbulence as seen in figure 14(*a*). For case A, the first mode-pair contains ≈17 % of the total energy,

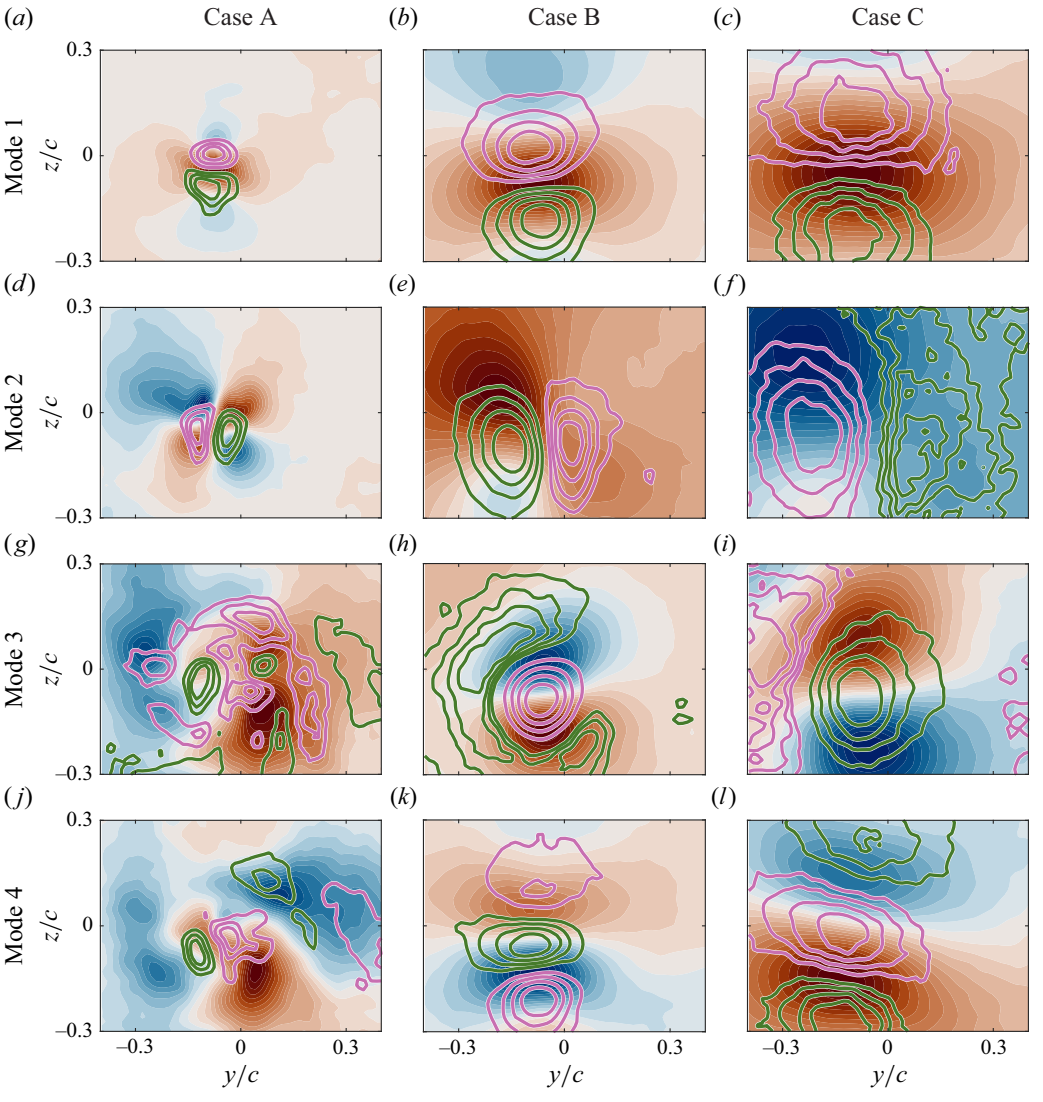

Figure 13. Spatial organisation of fluctuating fields corresponding to POD eigenmodes $n = 1$ (*a–c*), $n = 2$ (*d–f*), $n = 3$ (*g–i*) and $n = 4$ (*j–l*) for cases A (*a,d,g,j*), B (*b,e,h,k*) and C (*c,f,i,l*). Filled contours represent the component of POD spatial modes along the lift direction, Ψ_n^y (blue, positive; red, negative). Contour lines represent the vorticity-like term computed with both components of the respective POD spatial modes ($\Omega_n^x = \boldsymbol{\nabla} \times \boldsymbol{\Psi}_n(y, z)$; green, positive; pink, negative).

which increases to approximately 41 % for cases B and C. Given that the spatial modes of this mode-pair resemble helical displacement modes previously linked to wingtip vortex meandering (Edstrand *et al.* 2016; Chen *et al.* 2018*a*,*b*; Dghim *et al.* 2021), these two features observed in the POD analysis point towards the increase in meandering amplitude with the addition of FST discussed in § 4.2. The premultiplied spectra of the temporal coefficients of these modes in figure 14(*b–d*) contain a spectral signature comparable to that of the meandering motion shown in figure 12 as well.

The third and fourth spatial modes of case A (figures 13*g* and 13*j*) do not show any clear structures. Their relative energies have also dropped below 5 %. On the contrary,

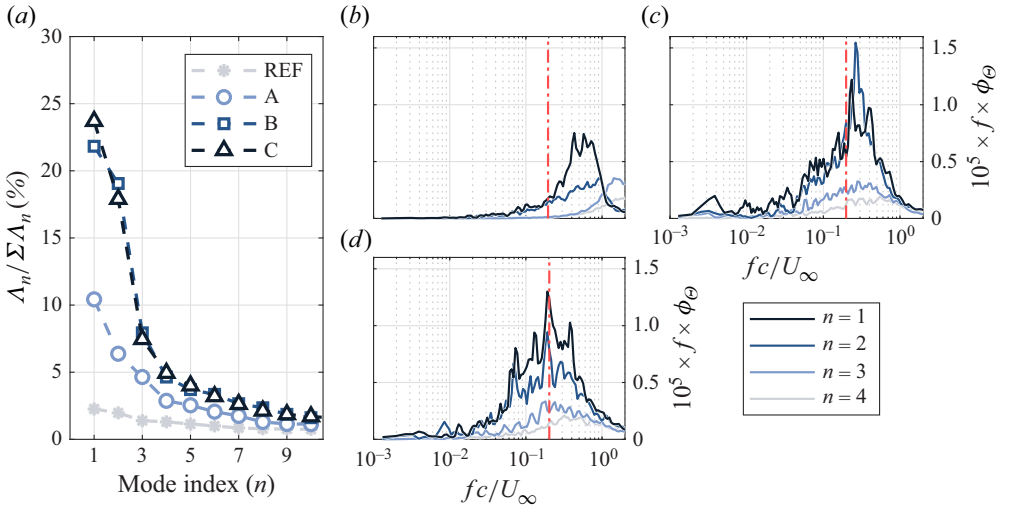

Figure 14. (*a*) Relative energies of the first 10 POD eigenmodes of all cases. (*b–d*) Premultiplied spectra of temporal coefficients of first four POD modes for cases A, B and C, respectively. Spectra of various modes are weighted with their relative energy for clarity. Dash–dotted line indicates normalised frequency of wing's vibration.

the third and fourth most energetic modes of cases B and C are vortex deformation modes. Specifically, the spatial organisation of the fourth mode resembles those resulting from the amplification of elliptical instabilities within the vortex tube with an azimuthal wavenumber of $m = 2$ (see Lacaze, Ryan & Le Dizes 2007). These modes represent only approximately 12 % of the total energy which is less than a third of the first two displacement modes. While the wing's increased vibration and/or the turbulence might be amplifying these deformation modes, the meandering motion is far stronger.

Interestingly, the orientation of structures in the most energetic modes across all three cases (figure 13*a–c*) suggests vortex displacement along the y direction, which coincides with the direction of the wingtip's deflection when FST is present. While this mode is only slightly more energetic than the second (≈5 %), this subtle preference in vortex displacement may suggest a potential influence of the wing's vibrations on vortex motion.

5. Interplay between FST, the wing's deflection and the wingtip vortex

The analysis in § 4 (and Appendix A), which follows established methodologies from previous studies on rigid finite wings, shows that the primary characteristics of wingtip vortices remain consistent even at higher FST levels than previously investigated and despite the wing being flexible. The agreement of the results here with the literature was not a foregone conclusion. However, notable deviations were observed in certain key aspects. Firstly, temporal variation in the size of the tip vortex was observed in § 4.1 which has not been reported previously. Secondly, the frequency band associated with vortex meandering was seen to drift towards the wing's vibration frequency with the addition of FST in §§ 4.3 and 4.4. Finally, indication of the meandering tending to be more in the direction of the wing's deformation was seen in § 4.2 and through the POD analysis in § 4.4. These observations indicate that the wing's flexibility does have an effect on the wingtip vortex. These effects are explored in greater detail in this section.

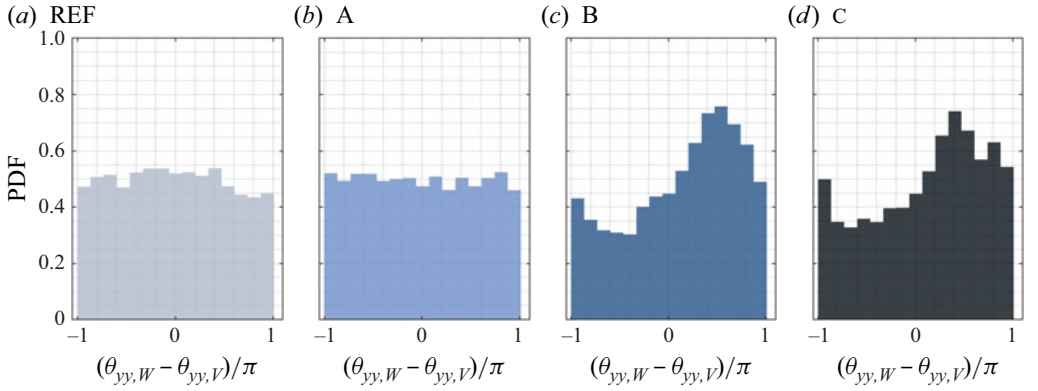

Figure 15. Probability density function of the instantaneous phase difference between the wing's deflection and vortex meandering motion. Here $\theta_{yy,W}$ and $\theta_{yy,V}$ are the instantaneous phases of the wing and vortex motion, respectively, obtained through the Hilbert transform.

5.1. *Wing and vortex motion*

The relationship between the wing's deflection and vortex meandering is investigated here. To do so adequately, a common reference signal, for both the motion of the wing and the tip vortex, is necessary. However, such a signal is not available in the current experimental set-up as both the wing and vortex were allowed to freely move with the incoming turbulence. The Hilbert transform, which is the convolution of a real valued signal with the Cauchy kernel $(1/\pi t)$, helps circumvent this issue with the Cauchy kernel playing the role of the common reference. In fact, this method was recently employed by Kushwaha *et al.* (2022) to assess the phase difference between the shear layers rolling up on either side of the potential core of a round jet subjected to transverse acoustic forcing. In the current study, the Hilbert transform was applied to the time series of the wingtip trailing edge displacement obtained from DIC and that of the conditioned vortex meandering from SPIV, which provided the instantaneous phase of the two motions along the y direction ($\theta_{yy,W}$ and $\theta_{yy,V}$, respectively) with respect to Cauchy kernel. The phase difference between the two signals was then computed and plotted as a probability distribution presented in figure 15.

In cases REF and A, the probability distributions show no dominant phase relation, with the occurrence of all phase differences having a probability of ≈ 0.5. For cases B and C, a dominant phase difference centred around 0.5π is evident, indicating a relation between the wing and vortex motions. Specifically, it shows that the wing's deflection leads that of the vortex meandering motion by 0.5π. This finding, that a dominant phase relation between the wing and vortex motions appears with FST, can be attributed to two already noted observations. First, the vortex motion moves towards longer wavelengths or smaller frequencies with FST, as discussed in §§ 4.3 and 4.4, which in the current experimental set-up also means a drift towards the wing's vibration frequency. Second, the wing's vibration amplitude increases significantly between cases REF and A, and cases B and C, as seen in figure 7(*a*). The results of this instantaneous phase-relation analysis follows the same trend, suggesting that the meandering motion of the vortex axis is correlated with the displacement of the wing at higher FST.

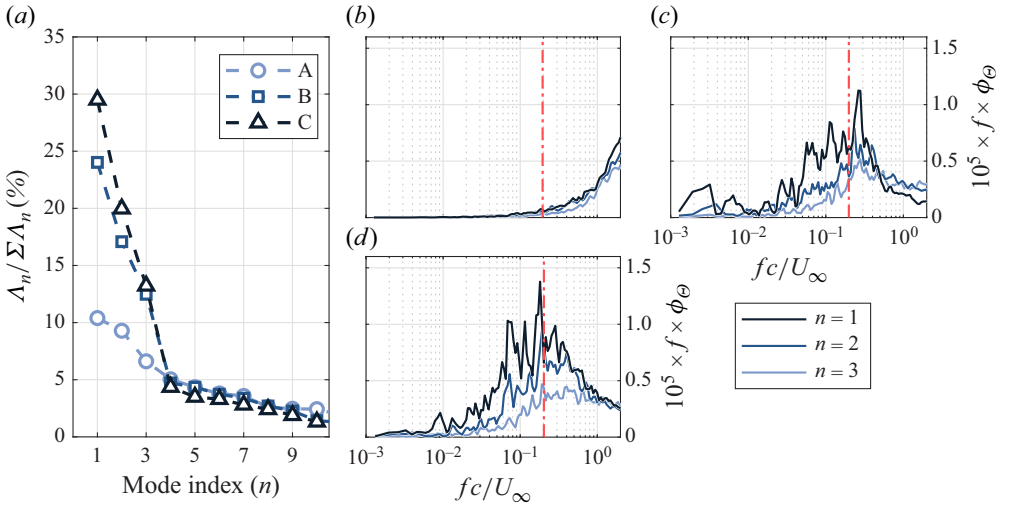

Figure 16. (*a*) Relative energies of the first 10 POD eigenmodes of all cases. (*b–d*) Premultiplied spectra of temporal coefficients of first three POD modes for cases A, B and C, respectively. Spectra of various modes are weighted with their relative energy for clarity. Dash–dotted line indicates normalised frequency of wing's vibration.

5.2. *Effect on the wingtip vortex*

It is imperative to also investigate the effect of the wing's deflection on the wingtip vortex itself in order to fully characterise its effect on the wake. The Hilbert transform analysis in § 5.1 shows that the wing's deflections has an effect on the vortex' motion. A similar trend was observed in the POD analysis of the full SPIV FOV presented in § 4.4. In that analysis, a substantial portion of the total energy was concentrated in the first mode pair, representing vortex meandering (≈17 % for case A, ≈41 % for cases B and C). In contrast, the third and fourth most energetic modes in cases B and C, resembling deformation modes, accounted for only ≈12 % of the total energy. To better isolate the effects on the vortex itself, it is necessary to remove the vortex core's meandering motion before performing POD, which is undertaken here. To this effect, velocity vectors within a square window of size $\pm 2r_c$ centred around the vortex centre were extracted from the original full-field time series. It is worth noting that the meandering component was not fully removed and the vortex did have some motion within the $\pm 2r_c$ interrogation window. Nevertheless, snapshot-POD was applied on this extracted time series of cases A, B and C, and only on the fluctuations of the transverse velocity components. Similar to the previous POD computation, the fluctuating velocity fields arranged in matrix form as $(Q = [(v - \hat{v}); (w - \hat{w})])$ are decomposed using (4.2). Once again, $\Psi_n(\hat{y}, \hat{z})$ are a set of empirical eigenfunctions (spatial POD modes) that contain information regarding the spatial organisation of various fluctuations with corresponding eigenvalues, Λ_n, representing the modal energy and temporal coefficients, $\Theta_n(t)$, with n being the mode number. It is worth noting that the modes are sorted in descending order of their relative modal energy here as well.

The relative energy of the first 10 most energetic POD modes corresponding to the three cases are presented in figure 16(*a*). In case A, the energy of subsequent modes decreases monotonically, with the first mode containing ≈10 % of the total energy. For test cases B and C, the energy of the first three POD modes is much higher compared with those in

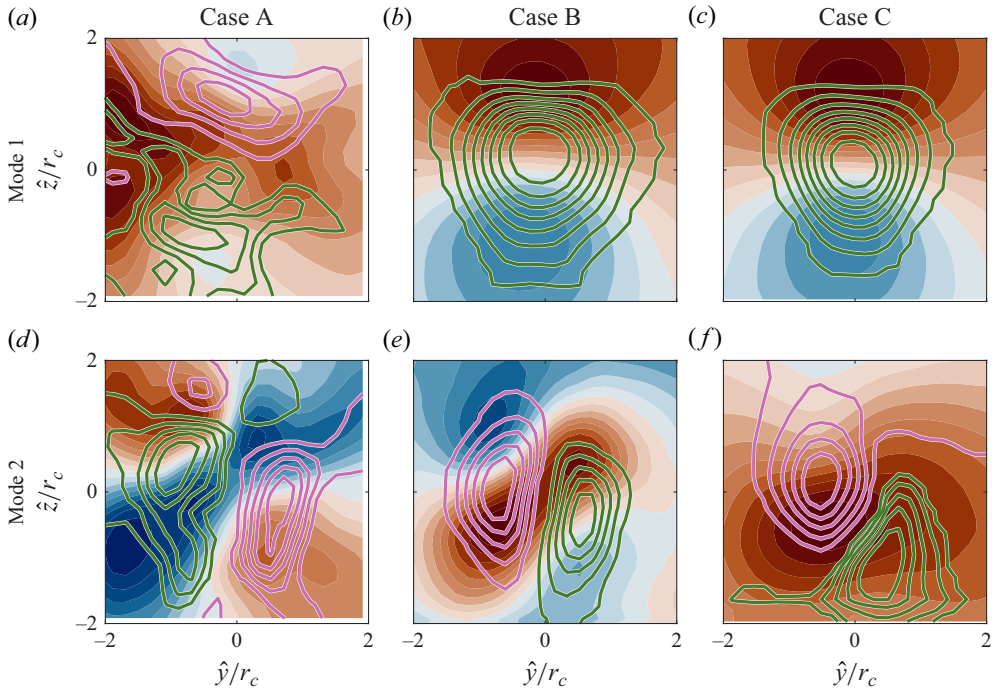

Figure 17. Spatial organisation of fluctuating fields corresponding to POD eigenmodes $n = 1$ (*a–c*) and $n = 2$ (*d–f*) for cases A (*a,d*), B (*b,e*) and C (*c,f*). Filled contours represent component of POD spatial modes along the lift direction, $\Psi_n^{\hat{y}}$ (blue, positive; red, negative). Contour lines represent the vorticity-like term computed with both components of the respective POD spatial modes ($\Omega_n^x = \nabla \times \Psi_n(\hat{y}, \hat{z})$; green, positive; pink, negative).

case A. The first modes contain ≈25 % and ≈30 % of the total energy in cases B and C, respectively, which is significantly higher compared with the first mode of case A. The results reported here (see § 4) and previous studies (Ghimire & Bailey 2017; Bailey *et al.* 2018; Ben Miloud *et al.* 2020) have demonstrated that increasing FST leads to a reduction in the vortex strength. Thus, the increase in the relative energy of the first three POD modes of cases B and C, while that of the other modes remaining almost constant (less than 1 % change from case A), cannot be due to the FST's action on the tip vortex. It can also not be due to the meandering motion as this has effectively been removed through the windowing around the vortex centre. This is rather attributed to the increased amplitude of the wing's deflection as will be discussed later.

Premultiplied spectra of the temporal coefficients of the first three POD modes corresponding to the three cases are shown in figure 16(*b–d*). Similar to figure 14(*b–d*), the spectra of individual modes are weighted by their relative energy to improve clarity. No dominant peaks are observed in the spectrum of case A (figure 16*b*). With further increase in FST, the frequency band with the maximum energy tends towards the vibration frequency of the wing, with the frequency peak in the spectrum almost at the wing's vibration frequency for case C (figure 16*d*). This spectral signature is expected to be from the deflections of the wing, indicating the effect it has on the vortex itself, separate from how the vortex meanders.

The spatial organisation of fluctuations are now looked into to elucidate these effects further. The $\hat{y}$ component of the spatial eigenfunctions of the first two POD modes for cases A, B and C are shown in figure 17 as filled contours. The modes of case A do not contain a distinct structure. This is in agreement with the spectra of the corresponding

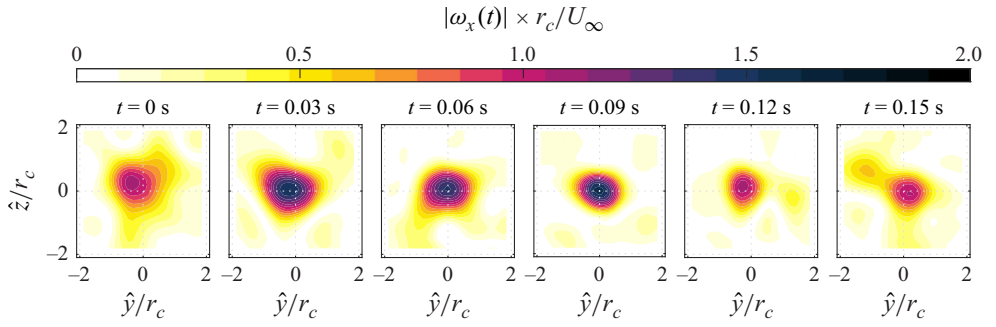

Figure 18. Normalised streamwise vorticity computed on six instantaneous velocity fields reconstructed from POD eigenmodes of case C. The six instantaneous fields represent one cycle of the wing's vibration at 6.2 Hz.

temporal coefficients not indicating a dominant frequency, but also with the full-field POD computation of this case where no clear structures were visible in the third most energetic mode (figure 13*g*) . In comparison, the first mode of cases B and C have a distinct pattern where the bottom-half is oriented along $+\hat{y}$ and the top is along $-\hat{y}$. Clear structures are also noticeable in the second modes of these two cases.

The cross product of the two components of the POD spatial modes ($\Omega_n^x = \nabla \times \Psi_n(\hat{y}, \hat{z})$), is computed and also shown in figure 17 as green and pink contour lines. In doing so, a distinct structure arises which indicates that the fluctuations represented by the first modes of cases B and C are organised in such a manner that it results in a rotational motion. This structure is similar to the elliptical structure in the third mode of cases B and C in the previous POD computation (figures 13*h* and 13*i*). In the second POD modes, two smaller rotational structures become evident through this process.

The motion of the vortex in the transverse plane or vortex meandering has been negated in the POD computation as previously explained. Thus, the fluctuations observed in the temporal coefficients' spectra in figure 16 cannot represent any vortex motion in the transverse plane. Instead, they are associated with the strength (and size) of the rotational structures in figure 17 (especially mode 1 of cases B and C) varying in time. Evidence of this can be found in figure 18, where the normalised streamwise vorticity of six instantaneous velocity fields spread along one cycle of the wing's vibration of 6.2 Hz is presented for the most turbulent case C. These instantaneous fields were reconstructed with the most energetic POD eigenmodes that account for 95 % of the total energy. The clear variation of the vorticity level and small changes to the vortex size with time are identifiable in these snapshots.

To get a global picture of this phenomenon, the instantaneous vortex circulation was computed from the reconstructed fields of all three turbulence cases within a square window of size $\pm r_c$ around the vortex centre. The premultiplied spectra of this quantity are presented in figure 19. The spectral content in case A is extremely low as expected, given the similar observations in figure 16(*b*). For cases B and C, fluctuations with maximum spectral content tend towards the wing's normalised vibration frequency, with it being almost same for case C, as was observed with the spectra of the vortex core's motion as well. This is further proof of the temporal variation of the wingtip vortex' strength in the current experimental study. Having demonstrated that these fluctuations, if not originating from the wing's deflection itself, are at least correlated with it, it can be safely said that the variation in the strength of the tip vortex in time must be a result of the wing's vibration.

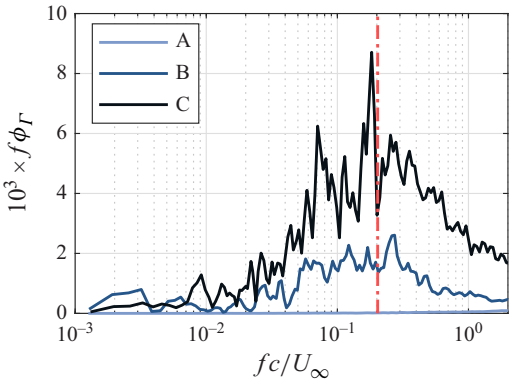

Figure 19. Premultiplied spectra of the circulation $\Gamma(t)$ computed from the reconstructed instantaneous velocity fields for the three turbulent cases. Dash–dotted (red) line indicates normalised frequency of wing's vibration. Note that the spectral content in case A is extremely low in comparison with cases B and C.

This observation can be explained as such. In the case of a rigid wing, the lift force generated by the wing and that perceived by the vortex is the same. Thus, a temporal variation in the vortex strength does not occur. This is in fact the observation with case A, where the vibration amplitude of the wing is at least three orders-of-magnitude lower than cases B and C as shown in figure 7(*a*) through the DIC measurements. The same does not hold when the vibration amplitude of the wing increases. In this scenario, when the wingtip is moving in the $+y$ direction or along the lift, the cumulative lift force that is perceived by the flow is in fact lower. When it is moving in the direction opposite to the lift (i.e. along $-y$), the cumulative force is higher. In fact, this temporal variation in the lift is represented in figure 5(*a*) by the vertical bars, which, as shown in figure 7(*b*), has a spectral peak at the wing's vibration frequency as well. This fluctuation in the perceived lift force must lead to a variation in the strength of the wingtip vortex but also its radius as seen in figure 9.

6. Conclusions

The impact of FST generated by an active turbulence grid on a flexible NACA 4412 finite wing and the ensuing wingtip vortex was investigated. To this effect, the wing's aerodynamic performance, structural deformation and the near-wake wingtip vortex were measured with several experimental methods. The measurements were conducted in a closed-loop wind tunnel at a chord-based Reynolds number of $Re_c = 1.4 \times 10^5$, with four different inflow conditions: a reference case without the active grid ($u'/U_\infty = 0.2\,\%$), a second case where the active grid was static ($u'/U_\infty = 3\,\%$) and two cases where the grid was operated with random sequences ($u'/U_\infty = 8\,\%$ and $u'/U_\infty = 13\,\%$). Hot-wire anemometry was used to examine the incoming flow characteristics, confirming transverse flow homogeneity for all cases.

Force balance measurements were employed to analyse the aerodynamic performance of the finite wing with increasing FST. The mean lift and drag curves showed an overall enhancement of the wing's aerodynamic performance, with a slight increase in maximum lift and delayed stall at higher FST. It is worth noting that there are very few measurements of the loads on finite wings subjected to homogeneous isotropic turbulence in the literature; therefore, these measurements are significant in their own right. The deformation of the wing was measured using DIC. Modal decomposition revealed

spanwise bending to be the dominant deflection. Spectral analysis of the deflections showed that the wing vibrated at its natural structural frequency at all inflow conditions. However, the amplitude of the vibrations increased with FST. Fluctuations at the same frequency as the wing's vibration were observed in the lift force as well.

Cross-stream SPIV was used to quantify the velocity fields in the wake, two chord lengths downstream of the wing's trailing edge, and to investigate the meandering behaviour of the wingtip vortex under these conditions. The statistics of the wingtip vortex agreed with previous experimental studies with rigid wings. A reduction in vortex strength with increasing FST, along with a small increase in diffusion and the size of the vortex was observed. The FST also had a significant impact on increasing meandering amplitude and the energy associated with vortex axis (i.e. vortex centre) motion at longer wavelengths or lower frequencies. It is relevant to note that these findings are a result of a vortex-centred reference frame. In the laboratory frame, there is an appearance of significant vortex diffusion with increasing incoming turbulence intensity; however, in the vortex' frame, these changes are small, and the laboratory frame results are in fact an artefact of the increase in vortex meandering blurring the averaged quantities over a larger physical area.

The footprint of the wing's deflection starts appearing in the vortex meandering, with the meandering frequency drifting towards that of the wing's deflections for the two most turbulent cases. In fact, for the most turbulent case, the frequency of these two parameters are identical. Instantaneous phase relation between these two signals obtained through the Hilbert transform showed that the vortex' meandering motion lagged the wing's deflection by $\approx 0.5\pi$. Proper orthogonal decomposition applied on velocity fields centred around the wingtip vortex further showed that the strength, and to a lesser degree the size, of the vortex varied along the deflection cycle of the wing. The spanwise bending of the finite wing was shown to induce fluctuations in the lift force. It is expected that this ultimately results in variations of the strength of the ensuing wingtip vortex giving it the appearance of pulsing in strength at a frequency correlated with the wing's deflection.

Declaration of interests. The authors report no conflict of interest.

Data availability statement. The data that support the findings of this study are openly available at DataverseNO: https://doi.org/10.18710/YW83LN.

Author contributions. Formal analysis, investigation, visualisation, writing (original draft) – S.Y. Formal analysis, investigation, methodology, visualisation, writing (original draft) – S.D. Formal analysis, investigation, methodology, supervision, writing (review and editing) – I.N. Investigation, writing (review and editing) – G.K.J. Investigation, writing (review and Editing) – R.K. Writing (review and editing) – M.C. Conceptualisation, funding acquisition, methodology, supervision, writing (review and editing) – R.J.H.

Appendix A. Azimuthal velocity profiles and vortex circulation

The ensemble average of the wingtip vortex azimuthal velocity as a function of the radial distance is presented in figure 20(*a*). The azimuthal velocity was determined by using the velocity components v and w in the Cartesian coordinate system and converting them into polar coordinates, as

$$u_\theta = w\cos(\theta) - v\sin(\theta)\,. \tag{A1}$$

This transformation then allowed for the calculation of the azimuthal velocity from the centre of the vortex along circular paths divided into 360°, with each degree representing a specific angular position defined by θ. Moreover, the radii of these circles were increased by 1 mm increments, allowing measurement at different distances from the vortex centre.

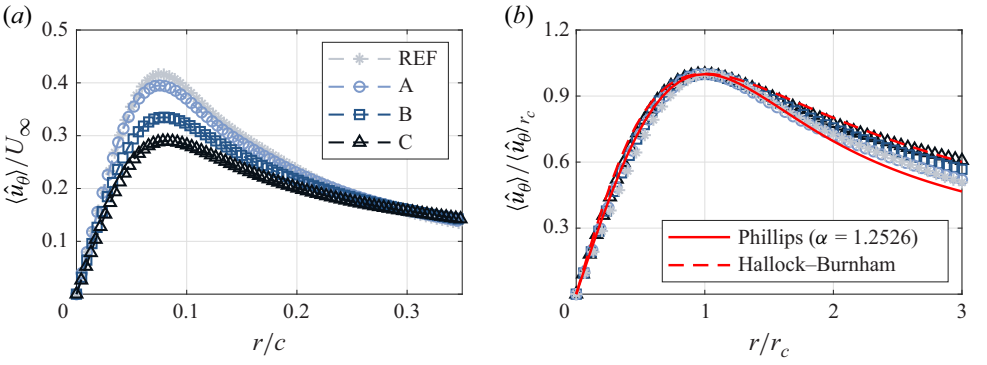

Figure 20. (*a*) Normalised azimuthal core velocity profiles for each turbulent case. (*b*) Comparison of the normalised core azimuthal velocity profiles for each turbulent case with the fitting curve of Phillips (1981).

The vortex size was characterised by the vortex core radius r_c. Finally, the velocities laying on a circular path at the same distance from the vortex centre were ensemble-averaged to study the evolution of the averaged azimuthal velocity ($\langle\hat{u}_\theta\rangle$) along the radial distance. This is shown in figure 20(*a*), which reveals a clear relationship between the azimuthal velocity peak and FST. The peak velocity decreases with increasing FST, leading to the velocity profiles becoming gradually flatter. This finding is consistent with the observation of Bailey *et al.* (2006) that, regardless of the level of turbulence, the azimuthal velocity in the outer core decreased with radial distance after reaching its peak, ultimately approaching an asymptotic constant value.

Figure 20(*b*) shows the evolution of the azimuthal velocity normalised by the azimuthal velocity at the core $u_\theta^{r_c}$ as a function of the radial distance normalised by the radius of the vortex core r_c. The experimental curves were compared with the Phillips (1981) model as suggested by Ben Miloud *et al.* (2020) to highlight the self-similar behaviour of the azimuthal velocity profiles, i.e.

$$\frac{u_\theta}{u_\theta^{r_c}} = \left(1 + \frac{1}{2\beta}\right)\frac{r_c}{r}\left(1 - \exp\left(-\beta\frac{r^2}{r_c^2}\right)\right), \tag{A2}$$

where $\beta = 1.2526$ is chosen to fit with the Lamb–Oseen model (Lamb & Caflisch 1993). A second comparison with the Hallock–Burnham model (Burnham & Hallock 1982) was also used, as suggested by Ghimire & Bailey (2017). The azimuthal velocity profile for this model is defined by

$$u_\theta = \frac{\Gamma_\infty}{2\pi r}\left(\frac{r^2}{r^2 + r_c^2}\right) \tag{A3}$$

where the freestream circulation Γ_∞ was chosen such that $u_\theta = u_\theta^{r_c}$ when $r = r_c$. It is observed that both the Phillips and Hallock–Burnham models fit the profiles reasonably well. The Phillips model was a good fit with the lowest FST cases in the outer core ($r > r_c$). However, as FST increased, the model that fit best in the outer core became the Hallock–Burnham model as can be seen in figure 20(*b*). These findings are consistent with Ghimire & Bailey (2017). While the profiles in the outer core showed some deviations from the Phillips model, the azimuthal velocity profiles for the experimental data in the inner core region were in good agreement with the Phillips model, indicating that the inner core structure of the vortex was self-preserving.

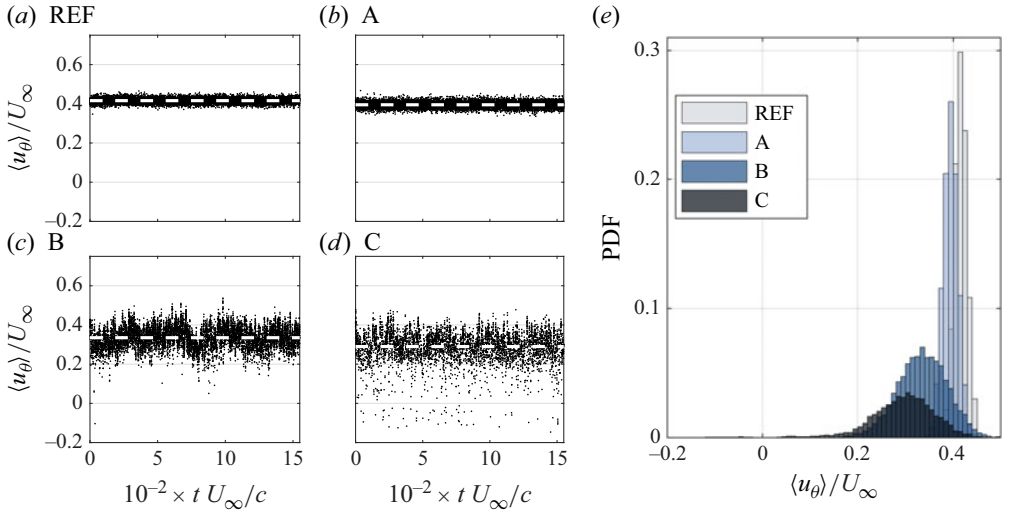

Figure 21. (*a–d*) Evolution of the azimuthal vortex velocity over time. (*e*) The PDF of the vortex azimuthal velocity.

Misaka *et al.* (2014) showed that during the initial vortex roll-up, the azimuthal velocity profile adhered to the Lamb–Oseen vortex model. However, after the completion of the roll-up process, the Hallock–Burnham model provided a more accurate representation of the vortex behaviour. Considering that the Phillips model shares similarities with the Lamb–Oseen model, it was inferred that the increase in FST enhanced the rate at which the vortex reached its fully developed structure. Given that, for the turbulence cases in the current study, the azimuthal velocity profile of the vortex matches the theoretical Phillips model well as seen in figure 20(*b*), models describing the interaction between vortex filaments and turbulence (for example, Stout & Hussain 2016) might be extended by incorporating the additional influence of the wing's deflection footprint. This footprint could be represented as a modulation imposed at the wing's dominant modal frequency. In this way, a model could be built to capture the essential physics of the current configuration, where turbulence, wing's deflection and vortex dynamics interact simultaneously.

In figure 21(*a–d*), time series plots of the core azimuthal velocity are presented. For the cases with lower turbulence, the maximum azimuthal velocity remained relatively stable around the mean value and followed a normal distribution with mean $u_\theta^{rc}/U_\infty = 0.4160$, as shown in figure 21(*e*). As FST increased, the deviation from the mean also increased, resulting in a much larger variation in azimuthal velocities for the most turbulent cases. Additionally, the farthest velocities from the mean in the most turbulent cases were biased towards lower velocities, causing a negatively skewed distribution. This effect can be seen in figure 21(*e*), where a decrease in the averaged maximum azimuthal velocity can be seen when increasing FST, accompanied with a stretching of the distribution towards lower azimuthal velocities. For case A, the average of the maximum azimuthal velocity decreased to $\langle u_\theta \rangle / U_\infty = 0.3950$. As for cases B and C, the averages were $\langle u_\theta \rangle / U_\infty = 0.3349$, and 0.2897, respectively. These results complement the results in figure 20 and align with Bailey *et al.* (2006) and Ghimire & Bailey (2017), as the authors also reported a reduction in maximum azimuthal velocity due to increasing FST.

Figure 22 shows the evolution of the circulation $\hat{\Gamma}$ normalised by the circulation at the vortex core with the radial distance from the centre of the vortex. The circulation was

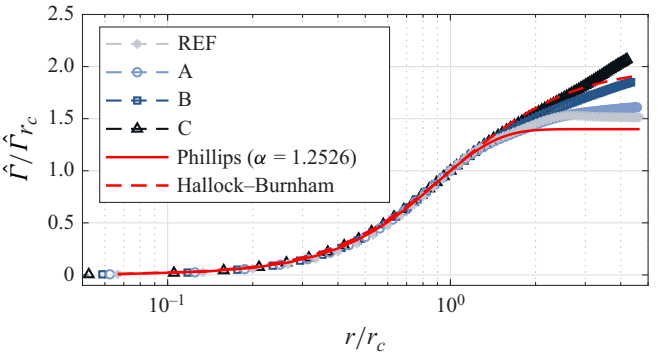

Figure 22. Normalised self-similar vortex circulation profiles for each turbulent case. Comparison with the Phillips (1981) and Burnham & Hallock (1982) models is also presented.

computed along a circular path at each radial position of interest r by

$$\Gamma(r) = 2\pi r u_\theta(r). \tag{A4}$$

For each case, the value for the circulation at the vortex core Γ_{r_c} was used to normalise the circulation and is presented in figure 22. In the inner core ($r/r_c < 1$), the circulation followed a parabolic function with the radius, indicating that the inner core was in approximately rigid-body rotation, as noted by Pentelow (2014). As the normalised radial distance increased, the circulation increased as well until it reached an inflection point at $r/r_c = 1$. Beyond this, the rate of increase starts to reduce as the vortex velocity field approaches an irrotational state outside the core region (Dghim, Ferchichi & Fellouah 2018). Increasing the FST led to a shift in the radial position where the circulation ratio first starts to decrease. In addition, the circulation ratio increased with FST, indicating possibly a reduction in circulation near the core radius and therefore an increase in vortex diffusion, in agreement with Ghimire & Bailey (2017) and Ben Miloud *et al.* (2020). Both Phillips and Hallock–Burnham models are also plotted in figure 22 for comparison. It is noteworthy that in the least turbulent case, the Phillips model provided a reasonable fit, while in the most turbulent case, the Hallock–Burnham model was better. This is consistent with the conclusions drawn earlier regarding the azimuthal velocity profiles and turbulence-enhancing evolution to the final state.

References

Ahmadi-Baloutaki, M., Carriveau, R. & Ting, D. 2014 Frequency analysis of a trailing vortex flow subjected to external turbulence. In *ASME International Mechanical Engineering Congress and Exposition, Proceedings (IMECE) 1*, V001T01A004.

Bailey, S., Pentelow, S., Ghimire, H., Estejab, B., Green, M. & Tavoularis, S. 2018 Experimental investigation of the scaling of vortex wandering in turbulent surroundings. *J. Fluid Mech.* **843**, 722–747.

Bailey, S. & Tavoularis, S. 2008 Measurements of the velocity field of a wing-tip vortex, wandering in grid turbulence. *J. Fluid Mech.* **601**, 281–315.

Bailey, S., Tavoularis, S. & Lee, B. 2006 Effects of free-stream turbulence on wing-tip vortex formation and near field. *J. Aircraft* **43** (5), 1282–1291.

Ben Miloud, K., Dghim, M., Fellouah, H. & Ferchichi, M. 2020 Free-stream turbulence interaction with a wing-tip vortex. *J. Wind Engng Indust. Aerodyn.* **206**, 104211.

Benedict, L. & Gould, R. 1996 Towards better uncertainty estimates for turbulence statistics. *Exp. Fluids* **22** (2), 129–136.

Bölle, T. 2024 On the linear response theory of vortex meandering and its statistical verification in experiments. *J. Fluid Mech.* **997**, A38.

Burnham, D.C. & Hallock, J.N. 1982 Chicago monostatic acoustic vortex sensing system, wake vortex decay. *Tech. Rep.*. Report No. DOT/FAA/RD-79-103, IV, United States. Federal Aviation Administration.

BÖLLE, T., BRION, V., COULIOU, M. & MOLTON, P. 2023 Experiment on jet–vortex interaction for variable mutual spacing. *Phys. Fluids* **35** (1), 015117.
CHEN, C., WANG, Z. & GURSUL, I. 2018*a* Experiments on tip vortices interacting with downstream wings. *Exp. Fluids* **59**, 1–24.
CHEN, C., WANG, Z. & GURSUL, I. 2018*b* Vortex coupling in trailing vortex-wing interactions. *Phys. Rev. Fluids* **3** (3), 034704.
CHEN, H. & JAWORSKI, J.W. 2020 Aeroelastic interactions and trajectory selection of vortex gusts impinging upon Joukowski airfoils. *J. Fluid. Struct.* **96**, 103026.
CHOW, J.S., ZILLIAC, G.G. & BRADSHAW, P. 1997 Mean and turbulence measurements in the near field of a wingtip vortex. *AIAA J.* **35** (10), 1561–1567.
COMTE-BELLOT, G. & CORRSIN, S. 1966 The use of a contraction to improve the isotropy of grid-generated turbulence. *J. Fluid Mech.* **25** (4), 657–682.
CRUZ MARQUEZ, R., MONNIER, J.C., TANGUY, G., COULIOU, M., BRION, V., CATTAFESTA, L. & DUPONT, P. 2021*a* An experimental study of a trailing vortex alleviation using an undulated trailing edge. In *AIAA Aviation Forum 2021–2562*. Session: Vortical/Vortex Flow Aerodynamics.
CRUZ MARQUEZ, R., MONNIER, J.C., TANGUY, G., COULIOU, M., BRION, V. & DUPONT, P. 2021*b* An experimental study of trailing vortex dynamics on cruise and high-lift wing configurations. In *AIAA Aviation Forum 2022-3390*. Session: Vortical/Vortex Aerodynamics II.
DEVENPORT, W., RIFE, M., LIAPIS, S. & FOLLIN, G. 1996 The structure and development of a wing-tip vortex. *J. Fluid Mech.* **312**, 67–106.
DGHIM, M., BEN MILOUD, K., FERCHICHI, M. & FELLOUAH, H. 2021 Meandering of a wing-tip vortex in a grid-generated turbulent flow. *Phys. Fluids* **33** (11),
DGHIM, M., FERCHICHI, M. & FELLOUAH, H. 2018 Mid-wake wing tip vortex dynamics with active flow control. *Exp. Therm. Fluid Sci.* **98**, 38–55.
DOWELL, E., EDWARDS, J. & STRGANAC, T. 2003 Nonlinear aeroelasticity. *J. Aircraft* **40** (5), 857–874.
EDSTRAND, A.M., DAVIS, T.B., SCHMID, P.J., TAIRA, K. & CATTAFESTA III, L.N. 2016 On the mechanism of trailing vortex wandering. *J. Fluid Mech.* **801**, R1.
FABRE, D., SIPP, D. & JACQUIN, L. 2006 Kelvin waves and the singular modes of the Lamb–Oseen vortex. *J. Fluid Mech.* **551**, 235–274.
FERNANDEZ, F., CLEAVER, D. & GURSUL, I. 2022 Unsteady aerodynamics of flexible wings in transverse gusts. *J. Fluid. Struct.* **108**, 103425.
GHIMIRE, H. & BAILEY, S. 2017 An experimental investigation of wing-tip vortex decay in turbulence. *Phys. Fluids* **29** (3), 037108.
GIUNI, M. & GREEN, R.B. 2013 Vortex formation on squared and rounded tip. *Aerosp. Sci. Technol.* **29** (1), 191–199.
GRAFTIEAUX, L., MICHARD, M. & GROSJEAN, N. 2001 Combining piv, pod and vortex identification algorithms for the study of unsteady turbulent swirling flows. *Meas. Sci. Technol.* **12** (9), 1422.
HEARST, R.J., BUXTON, O.R.H., GANAPATHISUBRAMANI, B. & LAVOIE, P. 2012 Experimental estimation of fluctuating velocity and scalar gradients in turbulence. *Exp. Fluids* **53**, 925–942.
HEARST, R.J. & LAVOIE, P. 2015 The effect of active grid initial conditions on high Reynolds number turbulence. *Exp. Fluids* **56** (10), 185.
HEYES, A.L., JONES, R.F. & SMITH, D.A.R. 2004 Wandering of wing-tip vortices. In *Proceedings of the 12th International Symposium on Applications of Laser Techniques to Fluid Mechanics*, Lisbon, Portugal, Paper, 35–33.
HOFFMANN, J.A. 1991 Effects of freestream turbulence on the performance characteristics of an airfoil. *Aiaa J.* **29** (9), 1353–1354.
HULTMARK, M. & SMITS, A.J. 2010 Temperature corrections for constant temperature and constant current hot-wire anemometers. *Meas. Sci. Technol.* **21**, 105404.
IFJU, P., JENKINS, D., ETTINGER, S., LIAN, Y., SHYY, W. & WASZAK, M. 2002 Flexible-wing-based micro air vehicles. In *40th AIAA Aerospace Sciences Meeting & Exhibit*, pp. 705.
KAY, N.J., RICHARDS, P.J. & SHARMA, R.N. 2020 Influence of turbulence on cambered and symmetrical airfoils at low Reynolds numbers. *AIAA J.* **58** (5), 1913–1925.
KILDAL, O., LI, L., HEARST, R.J., PETERSEN, Ø.W. & ØISETH, O. 2023 On the use of an active turbulence grid in wind tunnel testing of bridge decks. *J. Wind Engng Indust. Aerodyn.* **233**, 105331.
KROO, I., PRINZ, F., SHANTZ, M., KUNZ, P., FAY, G., CHENG, S., FABIAN, T. & PARTRIDGE, C. 2001 The mesicopter: a miniature rotorcraft concept phase ii final report.
KUSHWAHA, A.K., WORTH, N.A., DAWSON, J.R., GUPTA, V. & LI, L.K.B. 2022 Asynchronous and synchronous quenching of a globally unstable jet via axisymmetry breaking. *J. Fluid Mech.* **937**, A40.
LACAZE, L., RYAN, K. & LE DIZES, S. 2007 Elliptic instability in a strained Batchelor vortex. *J. Fluid Mech.* **577**, 341–361.

LAMB, H. & CAFLISCH, R. 1993 Hydrodynamics. Cambridge university press. ISBN 0521458684, 9780521458689.

LARSSEN, J.V. & DEVENPORT, W.J. 2011 On the generation of large-scale homogeneous turbulence. *Exp. Fluids* **50**, 1207–1223.

LI, L. & HEARST, R.J. 2021 The influence of freestream turbulence on the temporal pressure distribution and lift of an airfoil. *J. Wind Engng Indust. Aerodyn.* **209**, 104456.

MERTENS, C., FERNÁNDEZ, J.L.C., SODJA, J., SCIACCHITANO, A. & VAN OUDHEUSDEN, B.W. 2023 Nonintrusive experimental aeroelastic analysis of a highly flexible wing. *AIAA J.* **61** (7), 3062–3077.

MISAKA, T., OBAYASHI, S., STEPHAN, A., HOLZÄPFEL, F.N., GERZ, T. & NAKAHASHI, K. 2014 Numerical simulation of jet-wake vortex interaction. In *52nd Aerospace Sciences Meeting. AIAA 2014-0926*

NEUMANN, J. & MAI, H. 2013 Gust response: simulation of an aeroelastic experiment by a fluid–structure interaction method. *J. Fluid. Struct.* **38**, 290–302.

NORIHISA, M. & ISAO, S. 2002 Dynamics of a microflight mechanism with magnetic rotational wings in an alternating magnetic field. *J. Microelectromech. Syst.* **11** (5), 584–591.

PENTELOW, S.L. 2014 Wing-tip vortex structure and wandering. *PhD thesis*, Université d'Ottawa/University of Ottawa.

PHILLIPS, W.R.C. 1981 The turbulent trailing vortex during roll-up. *J. Fluid Mech.* **105**, 451–467.

SARPKAYA, T. & DALY, J.J. 1987 Effect of ambient turbulence on trailing vortices. *J. Aircraft* **24** (6), 309–404.

SCIACCHITANO, A. & WIENEKE, B. 2016 Piv uncertainty propagation. *Meas. Sci. Technol.* **27**, 084006.

SERRANO-AGUILERA, J., GARCÍA-ORTIZ, J., GALLARDO-CLAROS, A., PARRAS, L. & DEL PINO, C. 2016 Experimental characterization of wingtip vortices in the near field using smoke flow visualizations. *Exp. Fluids* **57** (8), 137.

SICOT, C., AUBRUN, S., LOYER, S. & DEVINANT, P. 2006 Unsteady characteristics of the static stall of an airfoil subjected to freestream turbulence level up to 16 %. *Exp. Fluids* **41** (4), 641–648.

SIROVICH, L. 1987 Turbulence and the dynamics of coherent structures. i. coherent structures. *Q. Appl. Maths* **45**, 561–571.

SOLIS, P., GARRIDO-MARTIN, M., DURAN, E., GUTIERREZ-CASTILLO, P. & DEL PINO, C. 2024 On the influence of spanwise deformation on lift coefficient and trailing vortices properties at low Reynolds number. *Phys. Fluids* **36** (3), 037122.

STOUT, E. & HUSSAIN, F. 2016 External turbulence-induced axial flow and instability in a vortex. *J. Fluid Mech.* **793**, 353–379.

SWALWELL, K., SHERIDAN, J. & MELBOURNE, W. 2001 The effect of turbulence intensity on stall of the naca 0021 aerofoil. In *14th Australasian Fluid Mechanics Conference Adelaide University*

TANG, D., GRASCH, A. & DOWELL, E.H. 2010 Gust response for flexibly suspended high-aspect ratio wings. *AIAA J.* **48** (10), 2430–2444.

THOMPSON, C., BILER, H., SYMON, S. & GANAPATHISUBRAMANI, B. 2023 Effects of integral length scale variations on the stall characteristics of a wing at high free-stream turbulence conditions. *J. Fluid Mech.* **974**, A9.

THOMPSON, C., BILER, H., SYMON, S. & GANAPATHISUBRAMANI, B. 2025 Aeroelastic wing performance in high-intensity freestream turbulence: integral length scale effects. *AIAA J.* **63** (5), 1789–1799.

VAN JAARSVELD, J.P.J., HOLTEN, A.P.C., ELSENAAR, A., TRIELING, R.R. & VAN HEIJST, G.J.F. 2011 An experimental study of the effect of external turbulence on the decay of a single vortex and a vortex pair. *J. Fluid Mech.* **670**, 214–239.

VERMEER, L.J., SØRENSEN, J.N. & CRESPO, A. 2003 Wind turbine wake aerodynamics. *Prog. Aerosp. Sci.* **39** (6), 467–510.

VITA, G., HEMIDA, H., ANDRIANNE, T. & BANIOTOPOULOS, C. 2020 The effect of the integral length scale of turbulence on a wind turbine aerofoil. *J. Wind Engng Indust. Aerodyn.* **204**, 104235.

WANG, S., ZHOU, Y., MAHBUB ALAM, M. & YANG, H. 2014 Turbulent intensity and reynolds number effects on an airfoil at low reynolds numbers. *Phys. Fluids* **26**, 115107.

WATKINS, S., MILBANK, J., LOXTON, B.J. & MELBOURNE, W.H. 2006 Atmospheric winds and their implications for microair vehicles. *AIAA J.* **44** (11), 2591–2600.

ZHANG, Z., WANG, Z. & GURSUL, I. 2020 Lift enhancement of a stationary wing in a wake. *AIAA J.* **58** (11), 4613–4619.

ZHANG, Z., WANG, Z. & GURSUL, I. 2022*a* Aerodynamics of a wing in turbulent bluff body wakes. *J. Fluid Mech.* **937**, A37.

ZHANG, Z., WANG, Z. & GURSUL, I. 2022*b* Effects of geometry of wings submerged in turbulent bluff-body wake. *AIAA J.* **61** (1), 241–254.